CENTRO DE INVESTIGACIONES
EN ÓPTICA, A.C.

Refractive index and geometrical thickness determination for optical media by Gaussian beam diffraction

Thesis submitted in partial fulfillment of the requirements for the Ph.D. degree in science

(Optics)

M. S. Octavio Olvera Rábago

Advisor:

Dr. Moisés Cywiak Garbarcewicz

"VERSIÓN DEFINITIVA"

December 2014
León, Guanajuato, México

Abstract

In this thesis we describe an optical, non-interferometric technique that allows characterizing high quality optical samples by measuring their main parameters: the refractive index and the geometrical thickness.

Our technique is based on characterizing a probe Gaussian beam transmitted through the sample under test. As the results of the measurements rely on tracking the referred parameters, we have devised a homodyne knife-edge detector to perform the measurements with the required accuracy. In this manner we characterize a thin pellicle consisting of a commercially available stretch film, obtaining a good agreement with the reported values of the manufacturer.

The relevance of our measurements relies on the difficulty to determine the refractive index and the geometrical thickness simultaneously by means of other techniques as it will be described in the introduction section. This is because the pellicle under test is very thin and it can easily suffer mechanical deformation or heating damage. As a consequence, a non-invasive low power technique is required. Besides, the center of the pellicle is vibrating constantly and if interferometric techniques are used, erroneous measurements would be obtained.

Once we accurately characterized the thin pellicle, we realized that a similar approach could be applied for characterizing optical plates. Even when there are a variety of techniques used to determine the refractive index and geometrical thickness of these plates, typically it is necessary to combine two techniques to determine them. In addition, focusing techniques which are commonly used are based on focusing a probe beam on the front and back surfaces of the plate. This is suitable for samples around one millimeter or more. However, when the plate is thinner than 200 microns it becomes difficult to discern the focusing at the surfaces thus obtaining misleading readings.

To alleviate the difficulties mentioned above, our proposal performs the measurements in a non-interferometric way and does not need to be combined

with any other technique which makes it suitable for the intended characterization. In this manner it was possible to characterize a high quality optical plate consisting of a cover glass.

For clarity, the presentation of this thesis is divided in six chapters. In the first chapter we present the introduction section on the subject. In chapter two the analytical description of our proposal is presented. In this section we include a review of the Fourier transform and the Fresnel diffraction integral which are widely used in this work. Chapter three provides the description of the homodyne detector, our experimental setup used to perform the measurements. In chapter four we describe the methodology we follow to characterize the pellicle in air. In chapter five we describe the characterization of the optical plate. In chapter six we present the conclusions obtained from this work. Finally the bibliography is presented.

Gratefullness

I want to thank Karely Chamé Fernández, my beloved girlfriend, partner and confident for all her support during this project called PhD. I appreciate her company and all the time we spend together. She inspires me and pushes me to be a better person every day.

To my family for all their care and support. To my parents Mario and Lupita and my sisters Carolina, Alexia and Melissa.

Special thanks to my advisor Dr. Moisés Cywiak Garbarcewicz for all his support, advice and patience. Without him this project could not be possible.

To my friends during the PhD: Joel Cervantes, Juan Manuel Franco, Moisés Padilla and David Cywiak. For all the laughs and funny moments together.

To my reviewers: Dr. David Moreno, Dr. Carlos Wiechers, Dr. Manuel Servín and Dr. Mauricio Flores for their valuable advice and suggestions.

To all the workers at Centro de Investigaciones en Óptica who helped me during this project.

To CONACYT for the financial support.

Contents

Chapter 1

Introduction

Accurate determination of the refractive index and geometrical thickness of optical samples has deserved special attention due to their vast field of applications [1-6]. Recently, novel research and new techniques in optical engineering, electronics, quality control in industry and biomedical applications, among others, demand higher accuracies on the measurement of these parameters because thinner and smaller components are constantly required.

This line of research led us to the case of an optical sample consisting on a thin pellicle supported only at its peripheral border. For brevity we denote these as “pellicles in air”. If one is interested in characterize properly the refractive index and geometrical thickness of these pellicles several difficulties arises.

At first impression one may think that interferometric techniques, which lead to nanometric resolutions on films deposited on some substrates [7-11] could be used. However, the center of the pellicle undergoes a piston-like continuous vibration even when using holographic tables in a controlled ambient. Therefore interferometric techniques can not be used as the fringe pattern will constantly vibrate resulting in erroneous measurements. An approach that avoids using interferometric techniques to alleviate the difficulty mentioned above can be found in [12]. The sample under test is placed between two polarizers and light is directed to the pellicle through one of the polarizers. This polarizer is tilted at different angles to be analyzed by the light that is transmitted through a second polarizer or analyzer. The angle that subtends the pellicle with the optical axis is the main parameter of the technique and has to be calculated with high accuracy. The refractive index and thickness of the sample are obtained by mathematical relations based on measuring at some specific angles. However, in the mentioned report the problem on the random and incessant pellicle vibrations that induce variations

on the angle is not considered. These vibrations in turn, depending on the distance of measurement may introduce severe variations on the readings.

It is also important to remark that as the pellicle under study is very thin it causes severe difficulties when optical tests are intended: the surface of the thin film should not be touched by any mechanical device as it can be easily damaged. If non-contact techniques based on laser probe beams are to be used, they should not exhibit high temperatures as the film can easily be deformed, which in consequence would result in misleading readings.

As it can be seen, the adequate characterization of the desired parameters for such sample represents a challenging problem for optical or non-contact techniques.

In this thesis we propose an alternative technique which is not based on interferometric principles to overcome these difficulties. This technique results more robust and provides the possibility to be applied in industrial environments. We demonstrate that it is possible to measure the local geometrical thickness and the refractive index of a transparent pellicle in air with high accuracy. This is accomplished by combining the diffractive properties of a transmitted Gaussian beam with the analytical equations of the light that propagates through a thin layer. Our technique is based on tracking the main parameters of a probe Gaussian beam transmitted through the sample under test at a plane of detection and, as the results of the measurements rely on following the referred parameters with high accuracy, we have devised a homodyne knife-edge detector that allows us to perform the measurements with the required accuracy. We also show that our measurement technique is immune to the inherent vibrations mentioned because the sample can be placed in the path of a focusing beam where piston-like movements of the pellicle do not affect the semi-width of the beam at a plane of detection. The feasibility of our proposal is confirmed by determining the refractive index and the local geometrical thickness at different spots of a commercially available stretch film. Our results are in good agreement with the values reported by the manufacturer of the stretch film.

By continuing with our research we noticed that there is a similar problem when it is attempted to characterize thin optical plates (ranging from 120 to 170 microns). These plates have several important industrial applications as flat panel displays, security window glasses and automobile windshields, among others, where their adequate performance depends on the accurate determination of their refractive index and geometrical thickness. However, as in the case of the pellicle, these plates also present several challenges when are tried to be characterized.

Nowadays a lot of techniques exist for characterizing these optical plates, however most of them require to combine two different techniques to determine the refractive index and the geometrical thickness. For example, low coherence interferometry (LCI) is combined with confocal microscopy [13-17], combinations of wave scanning interferometry (WSI) [18-22] or some type of focusing techniques based on a cyclic path optical configuration (CPOC) [23-24] which are based on focusing the probe beam on the surfaces of the sample under inspection to obtain two different equations from which the unknown parameters can be inferred. However, for measuring the geometrical thickness of a plate, conventionally it is necessary to focus a probe beam in their front and back surfaces. This is required in order to track the distance that a very precise mechanical device has traveled. This distance represents the geometrical thickness under measurement. However, when the sample is very thin, less than 200 microns, it results very difficult to determine when the probe beam has actually been focused as a circle of optical confusion inherently arises. As a consequence the mentioned techniques can be suitable for samples moderately thick (a few mm) and are difficult to be used for these thinner plates. As industry demands thinner plates constantly, alternative techniques are required.

For this reason, in this thesis we propose a technique for measuring simultaneously the local geometrical thickness and the refractive index of semi-transparent thin plates by means of the diffractive properties of a transmitted Gaussian beam. This approach can be considered as an extension of our proposal used for the pellicle. However, for this case the thin film equations can

not be applied due to the optical plate thickness (120-170 microns). Because of that our proposal is based on measuring the semi-width of the transmitted Gaussian beam when impinges normally to the sample and by determining the centroid position when the beam impinges obliquely by tilting the sample at different angles. Once again we perform our measurements with the homodyne detector to accurately characterize the parameters of the Gaussian beam.

As power measurements are not performed for this second case, the sample does not need to be highly transparent; this widens the range of applicability of our technique to semi-transparent samples. It is also important to remark that this proposal does not require any prior information of the sample under study.

Now that the focus of this thesis has been presented, it is convenient to provide the analytical description used for this work.

Chapter 2

Analytical description

In this section we describe our analytical approach. We consider convenient to begin with the definition of the Fourier and inverse Fourier transforms, which are related with the propagation of the probe beam as will be shown in a following section. The existence conditions and several mathematical properties of the transform are also provided [25]. Later the Fresnel diffraction integral is defined and several typical cases of interest are presented. Special attention is given to the case of the Gaussian distribution.

2.1 Fourier transform

2.1.1 Definition

For clarity and without loss of generality we assume the one dimensional definition of the Fourier transform. Let $f(x)$ an arbitrary function, complex in general, which depends on x, then its Fourier transform is defined as,

$$F\{g(x)\} = \int_{-\infty}^{\infty} g(x) \exp(-i 2\pi u x)\, dx, \tag{2.1}$$

where u is the Fourier or frequencies space. If the integral shown in (2.1) exists, it is possible to calculate the inverse Fourier transform as,

$$F^{-1}\{G(u)\} = \int_{-\infty}^{\infty} G(u) \exp(i 2\pi u x)\, du\,. \tag{2.2}$$

2.1.2 Existence conditions

For Eqs. (2.1-2.2) to be valid, it is necessary to fulfill the existence conditions, which are,

a. g must be absolutely integrable over the infinite (x, y) plane.
b. g must have only a finite number of discontinuities and a finite number of maxima and minima in any finite rectangle.
c. g must have no infinite discontinuities.

2.1.3 Mathematical properties

Now we will describe some of the basic mathematical properties of the Fourier transform for the two-dimensional case as follows:

1. Linearity theorem. The transform of a weighted sum of two (or more) functions is simply the identically weighted sum of their individual transforms, that is,

$$F\{ag + bh\} = aF\{g\} + bF\{h\}. \tag{2.3}$$

2. Similarity theorem. A stretch of the coordinates in the space domain (x, y) results in a contraction of the coordinates in the frequency domain (u, v), plus a change in the overall amplitude of the spectrum, that is,

$$F\{g(ax, by)\} = \frac{1}{|ab|} G\left(\frac{u}{a}, \frac{v}{b}\right), \tag{2.4}$$

considering that $F\{g(x, y)\} = G(u, v)$.

3. Shift theorem. Translation in the space domain introduces a linear phase shift in the frequency domain, that is,

$$F\{g(x - a, y - b)\} = G(u, v)\exp[-i\,2\pi(ua + vb)]. \tag{2.5}$$

4. Rayleigh's theorem (Parseval's theorem). The left hand integral can be interpreted as the energy contained in the waveform $g(x,y)$. This in turn means that the quantity $|G(u,v)|^2$ is an energy density in the frequency domain, that is,

$$\int_{-\infty}^{\infty}\int |g(x,y)|^2 dx\,dy = \int_{-\infty}^{\infty}\int |G(u,v)|^2 du\,dv. \tag{2.6}$$

5. Convolution theorem. The convolution of two functions in the space domain is equivalent to multiply their individual transforms and inverse transforming, that is,

$$F\left\{\int_{-\infty}^{\infty}\int g(\xi,\eta)h(x-\xi,y-\eta)d\xi\,d\eta = G(u,v)H(u,v)\right\}, \tag{2.7}$$

where $F\{h(x,y)\} = H(u,v)$.

6. Autocorrelation theorem. This theorem may be regarded as a special case of the convolution theorem in which we convolve $g(x,y)$ with $g^*(-x,-y)$, that is,

$$F\left\{\int_{-\infty}^{\infty}\int g(\xi,\eta)g^*(\xi-x,\,\eta-y)d\xi\,d\eta\right\} = |G(u,v)|^2, \tag{2.8a}$$

or similarly,

$$F\{|g(x,y)|^2\} = \int_{-\infty}^{\infty}\int G(\xi,\eta)G^*(\xi-u,\eta-v)\,d\xi\,d\eta. \tag{2.8b}$$

7. Fourier integral theorem. At each point of discontinuity of g, the two successive transforms yield the angular average of the values of g in a small neighborhood of that point. That is, the successive transformation and inverse transformation of a function yields that function again, except at points of discontinuity, that is,

$$FF^{-1}\{g(x,y)\} = F^{-1}F\{g(x,y)\} = g(x,y). \tag{2.9}$$

2.1.4 Fourier transform of a Gaussian distribution

As we mentioned at the beginning of this chapter, the Fourier transform is related with the propagation of the Gaussian beam, is then of interest to describe the Fourier of a Gaussian distribution.

If we consider a Gaussian distribution with semi-width equal to one, its Fourier transform is given by,

$$F\{\exp(-x^2)\} = \sqrt{\pi}\exp(-\pi^2 u^2). \tag{2.10}$$

For the more general case of a Gaussian distribution with semi-width r_0, its Fourier transform is given by,

$$F\left\{\exp\left(-\frac{x^2}{r_0^2}\right)\right\} = \sqrt{\pi}\, r_0 \exp(-\pi^2 r_0^2 u^2). \tag{2.11}$$

For simplicity in our calculations, in this work we use the following Gaussian distribution and its corresponding Fourier transform,

$$F\{\exp(-\pi x^2)\} = \exp(-\pi u^2). \tag{2.12}$$

Eq. (2.12) is said to be symmetric under Fourier transformation. And finally it is useful to obtain the following expression,

$$F\left\{\exp\left[-\pi(ax)^2\right]\right\}=\exp\left[-\pi\left(\frac{u}{a}\right)^2\right], \tag{2.13}$$

where a combination of the similarity theorem in Eq. (2.4) and the Eq. (2.12) has been used. In the following section we will use the property of Eq. (2.13) to show how a Gaussian distribution is propagated.

2.2 Fresnel diffraction integral

2.2.1 Definition

The propagation of an optical field can be evaluated by different approaches. In particular, one approach that gives very accurate results, being relatively simpler than other methods is the Fresnel diffraction integral. This theory is a scalar approach that can be applied if the following two conditions are valid:

1. The diffracting aperture must be large compared with the wavelength and,
2. The diffracting fields must not be observed too close to the aperture.

The Fresnel diffraction integral, for brevity we denote it just as Fresnel integral in the successive, permits to determine the amplitude distribution Ψ_F , often called image distribution, of a wave that propagates with an initial or object amplitude distribution Ψ_I from an initial plane with coordinates (x,y) up to a final plane with coordinates (ξ,η), both being mutually parallels and separated by a normal distance z as depicted in Fig. 2.1.

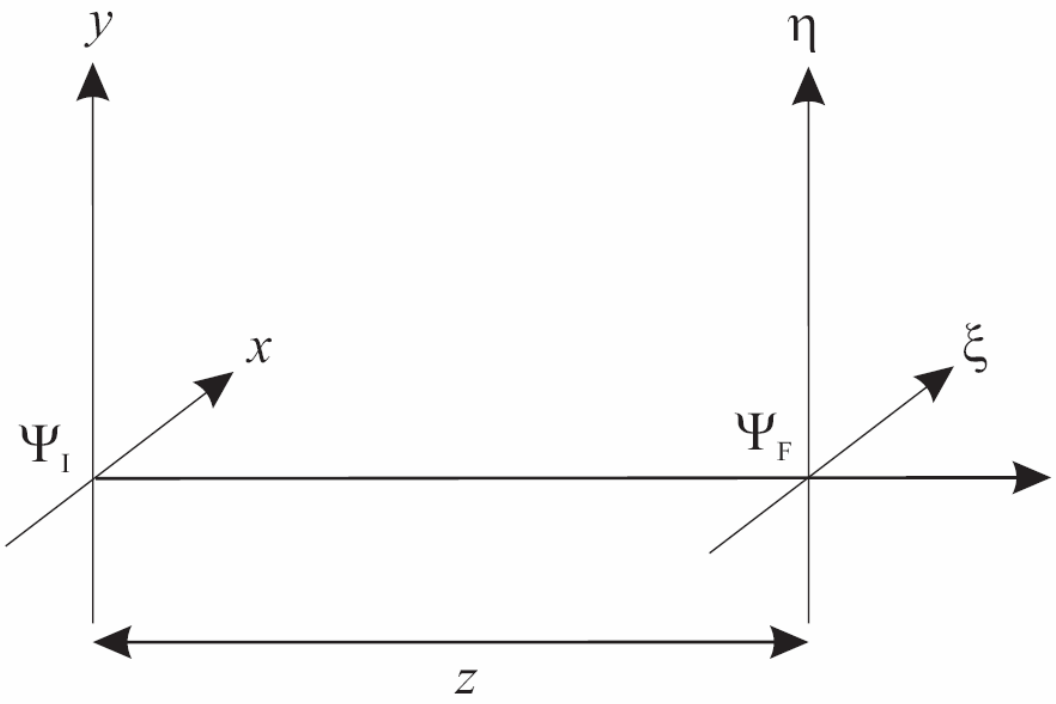

Fig. 2.1. Propagation of an object amplitude distribution Ψ_I at a plane with coordinates (x,y) resulting in an image amplitude distribution Ψ_F at a plane (ξ,η) by means of the Fresnel integral.

The analytical expression of the two-dimensional Fresnel integral can be expressed as,

$$\Psi_F(\xi,\eta)=\frac{\exp\left(i\frac{2\pi}{\lambda}z\right)}{i\lambda z}\int\int_{-\infty}^{\infty}\Psi_I(x,y)\exp\left\{i\frac{\pi}{\lambda z}\left[(x-\xi)^2+(y-\eta)^2\right]\right\}dx\,dy, \qquad (2.14)$$

where $i=\sqrt{-1}$ and λ is the illumination wavelength. For simplicity in our calculations and without loss of generality we can write Eq. (2.14) in its one-dimensional form as follows,

$$\Psi_F(\xi)=\frac{\exp\left(i\frac{2\pi}{\lambda}z\right)}{\sqrt{i\lambda z}}\int_{-\infty}^{\infty}\Psi_I(x)\exp\left[i\frac{\pi}{\lambda z}(x-\xi)^2\right]dx. \qquad (2.15)$$

By using the Fourier transform it is possible to rewrite Eq. (2.15) as,

$$\Psi_F(\xi) = \frac{\exp\left(i\frac{2\pi}{\lambda}z\right)}{\sqrt{i\lambda z}} \exp\left(i\frac{\pi}{\lambda z}\xi^2\right) F\left\{\Psi_I(x)\exp\left(i\frac{\pi}{\lambda z}x^2\right)\right\}. \tag{2.16}$$

By representing the final amplitude distribution Ψ_F in the form of Eq. (2.16) opens the possibility to give it a physical meaning. According to the convolution theorem in Eq. (2.7) the Fourier transform of a product results in the convolution of the individual transforms. In this manner this propagation involves the convolution of a quadratic phase with the Fourier transform of the object function.

2.2.2 Fraunhofer approximation

By considering the Fraunhofer approximation for far fields, valid when the distance z is considerably greater than the dimensions of the aperture, this is $z >> \frac{\pi}{2\lambda}\left(x^2 + y^2\right)$, Eq. (2.16) can be written as,

$$\Psi_F(\xi) \approx \frac{\exp\left(i\frac{2\pi}{\lambda}z\right)}{\sqrt{i\lambda z}} \exp\left(i\frac{\pi}{\lambda z}\xi^2\right) F\{\Psi_I(x)\}. \tag{2.17}$$

This equation shows that under Fraunhofer approximation the final amplitude distribution Ψ_F consists only in the Fourier transform of the object distribution. Now it is convenient to describe some of the typical cases of the Fresnel integral for amplitude distributions in the object plane and their corresponding amplitude distributions in the image plane.

2.2.3 Propagation of a rectangular distribution

The one-dimensional rectangle function of width A can be defined as,

$$rect\left(\frac{x}{A}\right)=\begin{cases}1 & if\,|x|<\frac{A}{2}\\ \frac{1}{2} & if\,|x|=\frac{A}{2}\\ 0 & otherwise\end{cases} \quad . \tag{2.18}$$

Fig. 2.2 shows a plot of the $rect(x)$, with $A=1$, this is a rectangle function with a width equal to one.

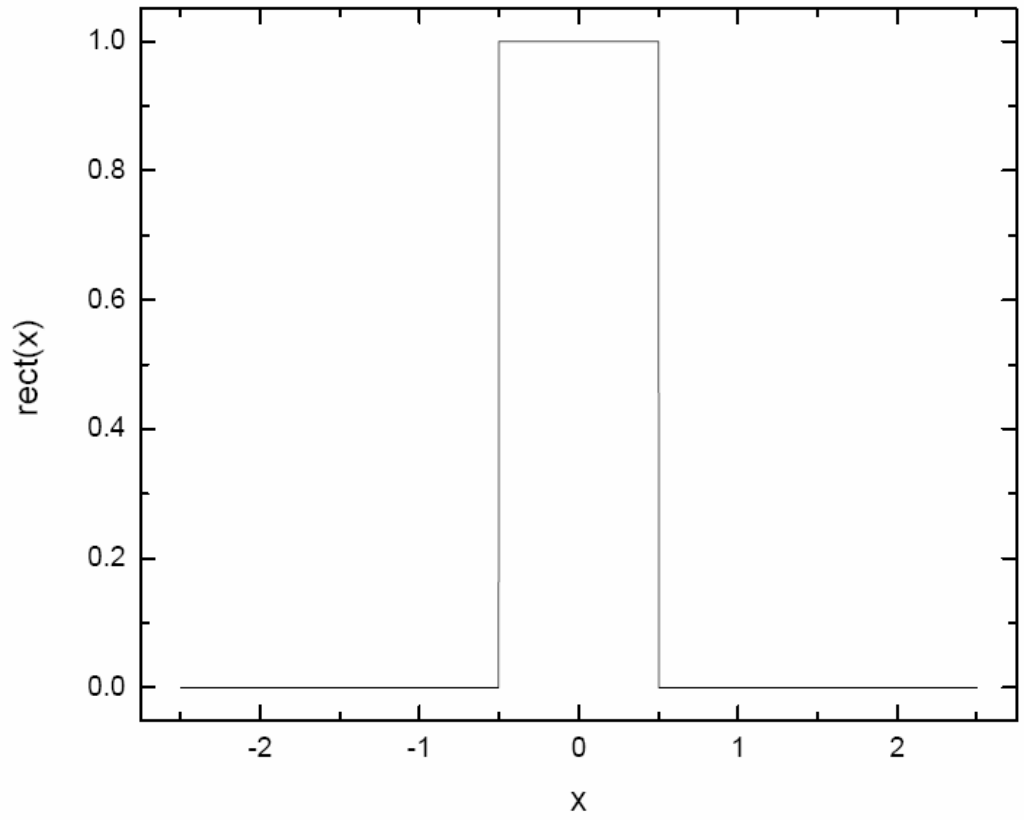

Fig. 2.2. Object distribution consisting of a rectangle function of width equal to one.

If $rect\left(\frac{x}{A}\right)$ is the initial amplitude distribution at the object plane, it is possible to calculate the final amplitude distribution at image plane by means of the Fresnel integral as follows,

$$\psi_F(\xi) = \frac{\exp\left(i\frac{2\pi}{\lambda}z\right)}{\sqrt{i\lambda z}} \int_{-\infty}^{\infty} rect\left(\frac{x}{A}\right) \exp\left[\frac{i\pi}{\lambda z}(x-\xi)^2\right] dx. \qquad (2.19)$$

By means of the Fresnel integral it is possible to calculate the amplitude distribution at any plane as long as the two conditions for scalar theory are fullfilled. Fig 2.3 depicts a plot of the image distribution amplitude when the rectangle function is propagated a distance of 5 cm. u represents the frequency space. As for this illustrative case we are interested only in the shape of the plot, the amplitude has been normalized for all the examples.

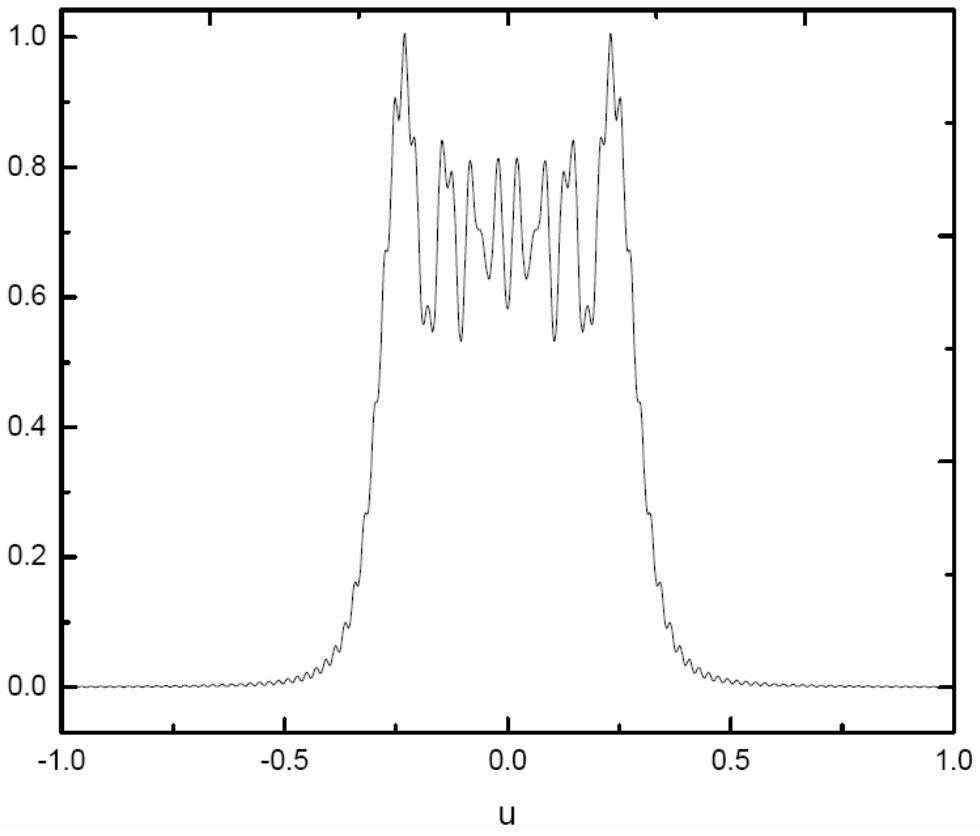

Fig. 2.3. Propagation of an object distribution consisting of a rectangle function by means of the Fresnel integral at a distance of 5 cm.

Fig. 2.4 shows the image amplitude distribution at a distance of 25 cm,

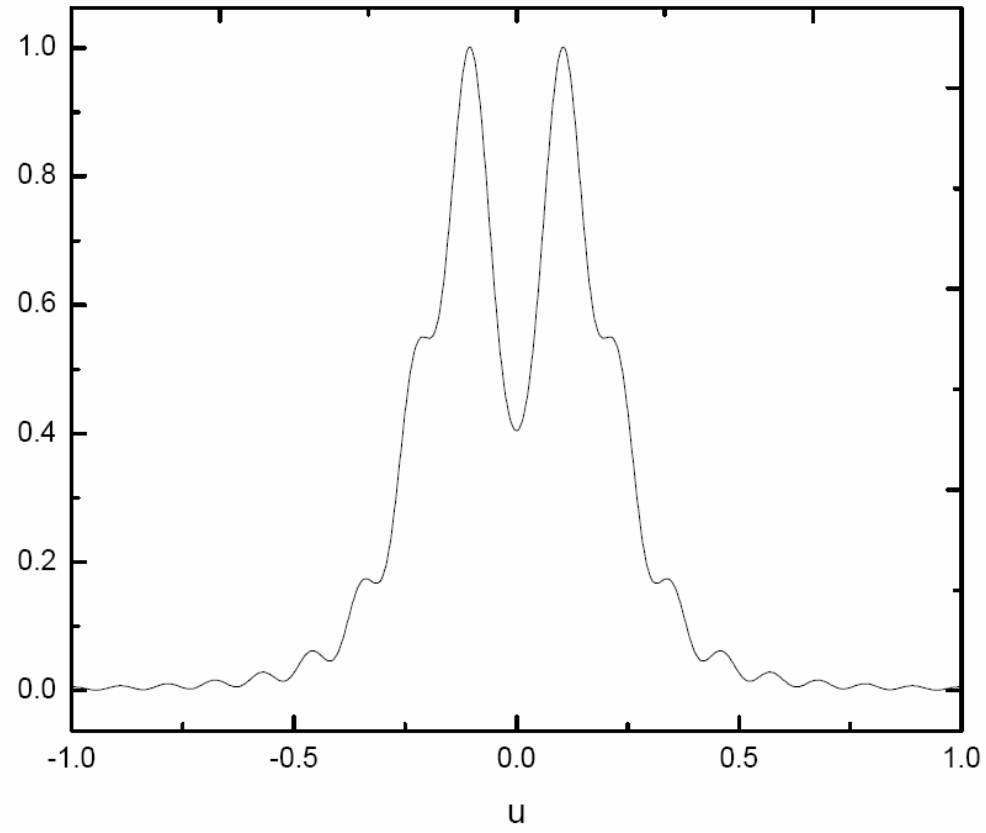

Fig. 2.4. Propagation of an object distribution consisting of a rectangle function by means of the Fresnel integral at a distance of 25 cm.

As mentioned, if the Fraunhofer approximation for far field is considered, the integral in Eq. (2.19) is simplified to the following equation,

$$\Psi_F(\xi) \approx \frac{\exp\left(i\frac{2\pi}{\lambda}z\right)}{\sqrt{i\lambda z}} \exp\left(i\frac{\pi}{\lambda z}\xi^2\right) F\left\{rect\left(\frac{x}{A}\right)\right\}, \tag{2.20}$$

which can be solved exactly resulting in,

$$\Psi_F(\xi) = \frac{\exp\left(i\frac{2\pi}{\lambda}z\right)}{\sqrt{i\lambda z}} \exp\left(i\frac{\pi}{\lambda z}\xi^2\right) A\, sinc\left(A\frac{\xi}{\lambda z}\right), \tag{2.21}$$

where the sinc function in Eq. (2.21) is defined as,

$$sinc(x) = \frac{\sin(\pi x)}{\pi x}. \tag{2.22}$$

Fig 2.5 shows a plot of the sinc function obtained at a distance of 1 m.

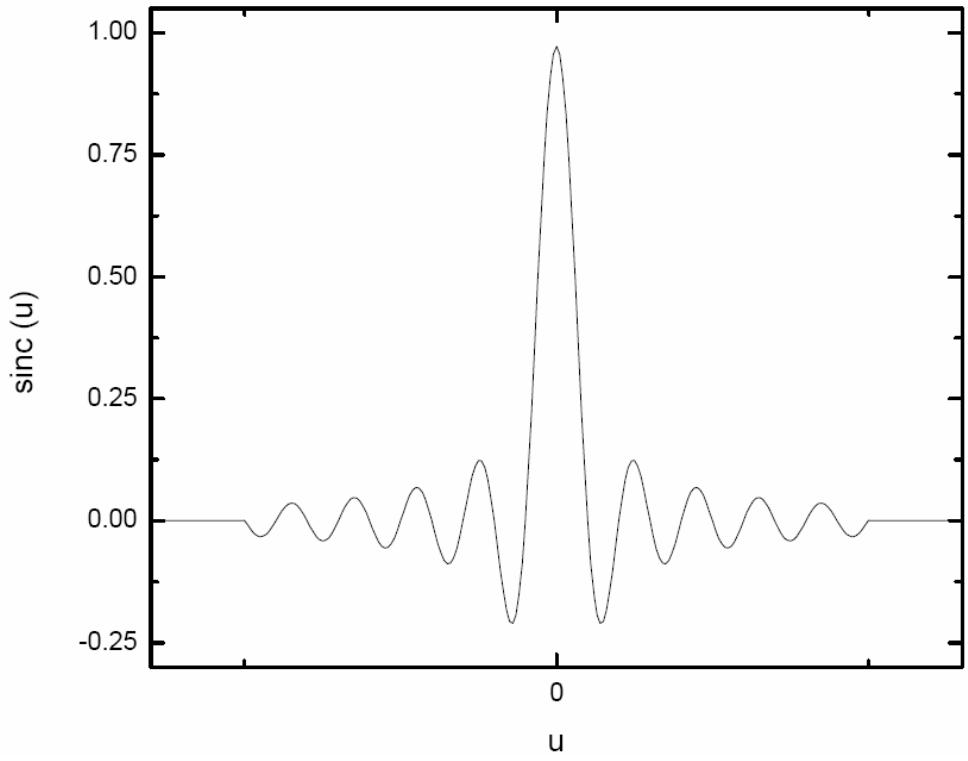

Fig. 2.5. Propagation of an object distribution consisting of a rectangle function by means of the Fresnel integral at a distance of 1 m. For this case the Fraunhofer approximation is considered.

2.2.4 Propagation of a Gaussian distribution

As we are interested in analyze the beam profile of a He-Ne laser for our experimental setup, it is convenient to describe the Gaussian beam distribution. We begin our analysis with the simplest case: a Gaussian function at the beam waist, this means that the equation will contain a Gaussian exponential term, but no an imaginary quadratic exponential which would correspond to a convergent or divergent phase. The analytical equation for this case, at the output of the laser at a plane (x) is given by,

$$\Psi(x) = A\exp\left(-\frac{x^2}{r_0^2}\right), \tag{2.23}$$

where A is a constant amplitude and r_0 is the beam semi-width. Fig. 2.6 depicts the Gaussian distribution shown in Eq. (2.23) for the case of amplitude equal to one and amplitude semi-width equal to one micron.

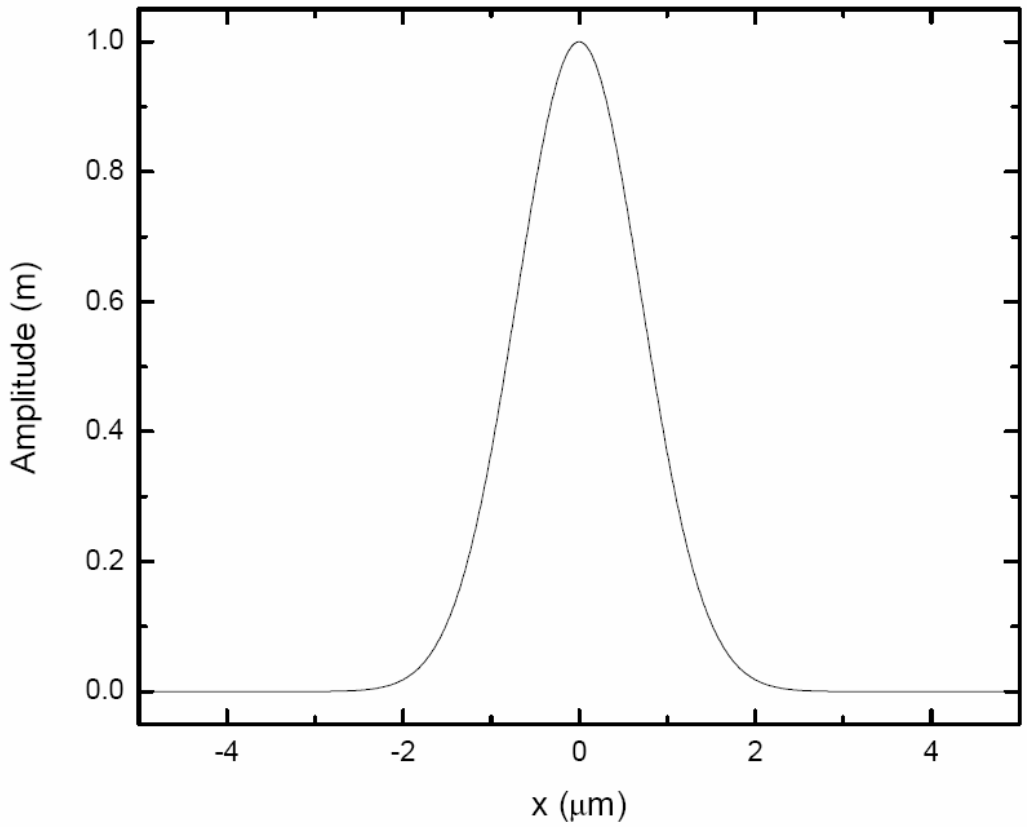

Fig. 2.6. Gaussian beam distribution with amplitude equal to one and semi-width equal to one micron.

If we now propagate this beam distribution up to another plane with coordinate (ξ) separated a distance z, by using the Fresnel integral it follows that,

$$\Psi_F(\xi)=\frac{\exp\left(i\frac{2\pi}{\lambda}z\right)}{\sqrt{i\lambda z}}\int_{-\infty}^{\infty}A\exp\left(-\frac{x^2}{r_0^2}\right)\exp\left[i\frac{\pi}{\lambda z}(x-\xi)^2\right]dx, \tag{2.24}$$

and according to Eq. (2.17) we can write,

$$\Psi_F(\xi)=\frac{A}{\sqrt{i\lambda z}}\exp\left(i\frac{2\pi}{\lambda}z\right)\exp\left(i\frac{\pi}{\lambda z}\xi^2\right)F\left\{\exp\left[-\pi\left(\sqrt{\frac{\lambda z-i\pi r_0^2}{\pi r_0^2\lambda z}}x\right)^2\right]_{\frac{\xi}{\lambda z}}\right\}. \tag{2.25}$$

Solving the Fourier transform and simplifying terms we obtain,

$$\Psi_F(\xi) = A_1 \exp\left(-\frac{\xi^2}{r^2}\right)\exp\left(i\beta\xi^2\right), \tag{2.26}$$

where,

$$A_1 = A\frac{\exp\left(i\dfrac{2\pi z}{\lambda}\right)}{\sqrt{i\lambda z}}\sqrt{\frac{\pi r_0^2 \lambda z}{\lambda z - i\pi r_0^2}}. \tag{2.27a}$$

$$r = \frac{\sqrt{\lambda^2 z^2 + \pi^2 r_0^4}}{\pi r_0}. \tag{2.27b}$$

$$\beta = \frac{\pi}{\lambda z}\left(1 - \frac{\pi^2 r_0^4}{\lambda^2 z^2 + \pi^2 r_0^4}\right). \tag{2.27c}$$

Eq. (2.26) shows that the distribution obtained after the propagation is also a Gaussian at plane ξ. In Eqs. (2.27) A_1 is the complex amplitude of the beam, r is the corresponding semi-width of the beam and β is the quadratic phase. Physically the second term in Eq. (2.26) is a real exponential which keeps the Gaussian behavior of the initial Gaussian distribution and the third term, the exponential with imaginary argument, represents a divergent spherical wave.

It can be noticed that Eq. (2.26) is complex, to plot this distribution we can obtain its corresponding intensity profile. The intensity distribution is given by,

$$I_F(\xi) = |A_1|^2 \exp\left(-2\frac{\xi^2}{r^2}\right), \tag{2.28}$$

where the intensity semi-width and the amplitude semi-width are related simply by,

$$r_A = \sqrt{2}\, r_I. \tag{2.29}$$

Fig. 2.7 depicts a plot of the intensity Gaussian profile.

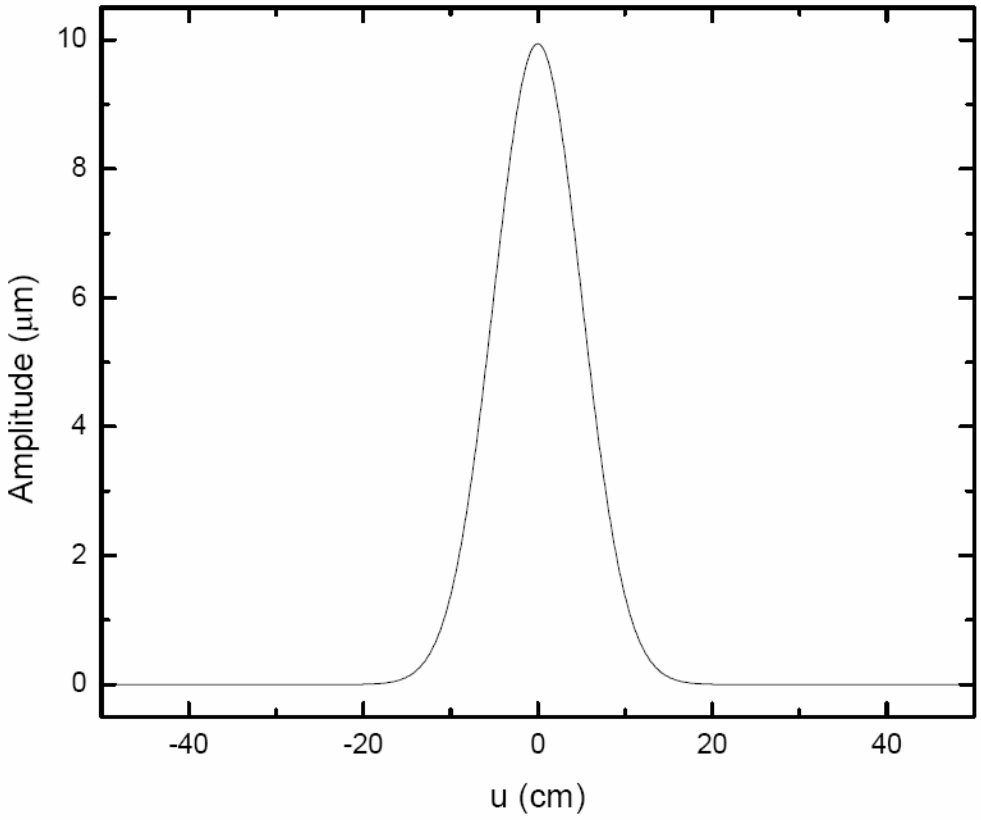

Fig. 2.7. Intensity Gaussian profile for a propagated Gaussian beam.

From the plot in Fig. (2.7), it can be noticed that the amplitude has been decreased drastically with respect that shown in Fig. (2.6), and accordingly the semi-width of the propagated profile has been increased from microns up to centimeters. The semi-width increases following Eq. (2.27b) and in Fig. 2.8 a plot of the semi-width as a function of the distance of propagation is depicted.

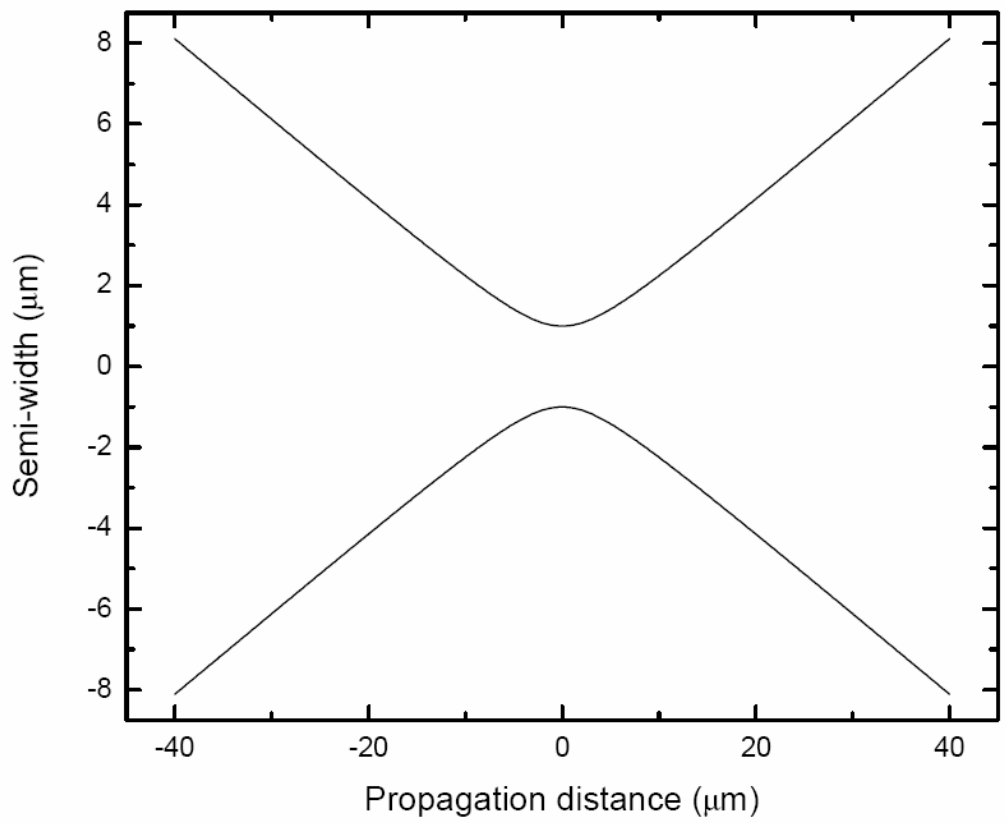

Fig. 2.8. Plot of the semi-width of the beam as a function of the distance of propagation. Zero distance is known as the beam waist, this means the place at which the semi-width exhibits a minimum.

2.2.5 Propagation of a Gaussian function with convergent quadratic phase

Now that we have described the Gaussian distribution at the beam waist, it is convenient for our purposes to analyze the more general case of a Gaussian distribution multiplied by a convergent quadratic phase as described in Eq. (2.30),

$$\Psi(x) = A\exp\left(-\frac{x^2}{r_0^2}\right)\exp\left(-i\beta x^2\right). \tag{2.30}$$

The expression in Eq. (2.30) can be interpreted as the Gaussian distribution after a focusing lens which introduces the convergent quadratic phase. By means of the Fresnel integral we write,

$$\Psi_F(\xi)=\frac{\exp\left(i\frac{2\pi}{\lambda}z\right)}{\sqrt{i\lambda z}}\int_{-\infty}^{\infty}A\exp\left(-\frac{x^2}{r_0^2}\right)\exp\left(-i\beta x^2\right)\exp\left[i\frac{\pi}{\lambda z}(x-\xi)^2\right]dx\,. \tag{2.31}$$

Eq. (2.31) can be written in terms of a Fourier transform as follows,

$$\Psi_F(\xi)=\frac{A}{\sqrt{i\lambda z}}\exp\left(i\frac{2\pi}{\lambda}z\right)\exp\left(i\frac{\pi}{\lambda z}\xi^2\right)F\left\{\exp\left[-\pi\left(\sqrt{\frac{\lambda z+ir_0^2(\beta\lambda z-\pi)}{\pi r_0^2\lambda z}}x\right)^2\right]\right\}_{\frac{\xi}{\lambda z}}. \tag{2.32}$$

In a similar way as it was done before in Eq. (2.26), it is possible to obtain an overall expression for Ψ_F, however for this case we are interested only in the semi-width. This is given by,

$$r=\frac{\sqrt{\lambda^2z^2+r_0^4(\beta\lambda z-\pi)^2}}{\pi r_0}. \tag{2.33}$$

The semi-width in Eq. (2.33) will be used later in the section of the characterization of the pellicle in air. Now that we have described the propagation of a Gaussian beam through a distance of propagation z, it will be useful for our purposes to describe the propagation through two or more successive planes that will be used in this work.

2.2.6 Propagation through two planes

In this section we analyze two successive propagations, the first one from the initial plane up to an intermediate plane, and the second one from this intermediate plane up to the final plane. For brevity of the equations, our description is one-dimensional.

In Fig. 2.9 the object field distribution $f(x)$ is located at plane x and it propagates up to a plane ξ separated a distance z_1. At this plane a new field distribution is found by means of the Fresnel integral, then it propagates again to a final plane x_F which is separated a distance z_2.

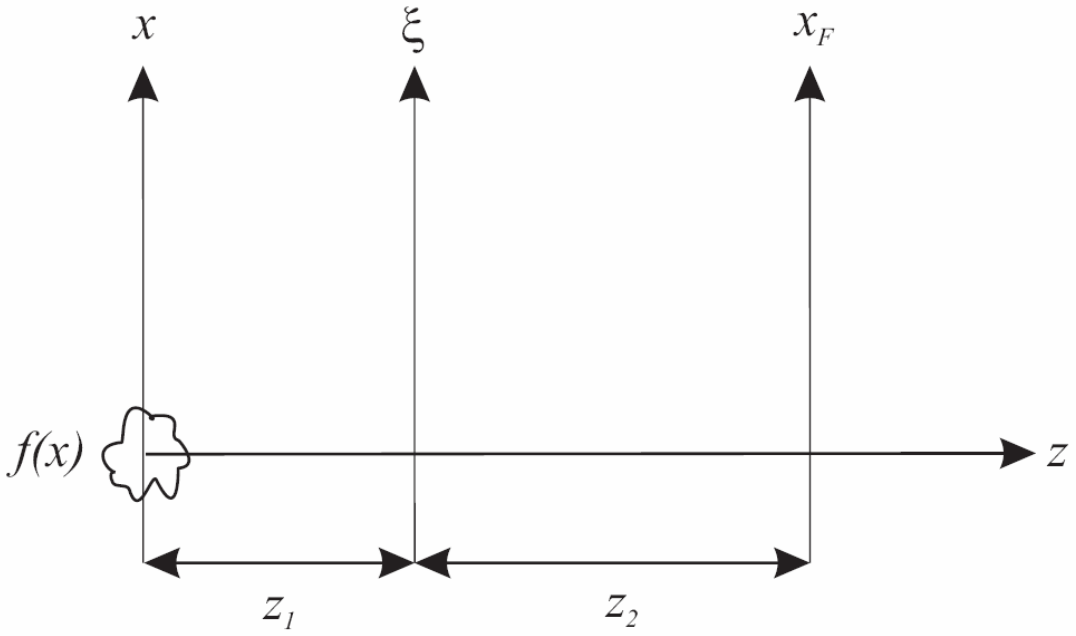

Fig. 2.9. Field distribution $f(x)$ at plane x which is propagated to a plane ξ separated a distance z_1 and finally up to a plane x_F separated a distance z_2.

It is expected that the same final field distribution can be obtained by a single propagation from plane x up to plane x_F, this can be represented mathematically by,

$$\int_{-\infty}^{\infty}\left\{\int_{-\infty}^{\infty} f(x)\exp\left[i\frac{\pi}{\lambda z_1}(x-\xi)^2\right]dx\right\}\exp\left[i\frac{\pi}{\lambda z_2}(\xi-x_F)^2\right]d\xi=\int_{-\infty}^{\infty} f(x)\exp\left[i\frac{\pi}{\lambda(z_1+z_2)}(x-x_F)^2\right]dx.$$

(2.34)

According to Eq. (2.15) these propagations are,

$$\frac{\exp(ikz_1)}{\sqrt{i\lambda z_1}}\frac{\exp(ikz_2)}{\sqrt{i\lambda z_2}}\iint f(x)\exp\left[i\frac{\pi}{\lambda z_1}(x-\xi)^2\right]\exp\left[i\frac{\pi}{\lambda z_2}(\xi-x_F)^2\right]dxd\xi,$$

(2.35)

where $k=\frac{2\pi}{\lambda}$ is the wave-number. Developing and grouping terms it follows that,

$$\frac{\exp[ik(z_1+z_2)]}{i\lambda\sqrt{z_1z_2}}\exp\left(i\frac{\pi}{\lambda z_2}x_F^2\right)\int dx\,f(x)\exp\left(i\frac{\pi}{\lambda z_1}x^2\right)F\left\{\exp\left[-\frac{\pi}{i\lambda}\left(\frac{z_1+z_2}{z_1z_2}\right)\xi^2\right]\right\}_{\frac{x}{\lambda z_1}+\frac{x_F}{\lambda z_2}},$$

(2.36)

and by solving the Fourier transform we obtain,

$$\frac{\exp[ik(z_1+z_2)]}{i\lambda\sqrt{z_1z_2}}\exp\left(i\frac{\pi}{\lambda z_2}x_F^2\right)\int dx\,f(x)\exp\left(i\frac{\pi}{\lambda z_1}x^2\right)\sqrt{\frac{i\lambda z_1z_2}{z_1+z_2}}\exp\left[-i\frac{\pi\lambda z_1z_2}{z_1+z_2}\left(\frac{x}{\lambda z_1}+\frac{x_F}{\lambda z_2}\right)^2\right].$$

(2.37)

It follows that,

$$\frac{\exp[ik(z_1+z_2)]}{\sqrt{i\lambda(z_1+z_2)}}\exp\left[i\frac{\pi}{\lambda z_2}\left(1-\frac{z_1}{z_1+z_2}\right)x_F^2\right]\int f(x)\exp\left[i\frac{\pi}{\lambda z_1}\left(1-\frac{z_1}{z_1+z_2}\right)x^2\right]\exp\left[-i2\pi\frac{x_F}{\lambda(z_1+z_2)}x\right]dx,$$

(2.38)

and finally it can be seen that,

$$\frac{\exp[ik(z_1+z_2)]}{\sqrt{i\lambda(z_1+z_2)}}\int f(x)\exp\left[i\frac{\pi}{\lambda(z_1+z_2)}(x-x_F)^2\right]dx. \tag{2.39}$$

In Eq. (2.39) the total distance the beam propagates is z_1+z_2 and the propagation is performed from plane x up to plane x_F, where the plane ξ vanishes for this final expression as expected.

2.2.7 Propagation through media with refractive index n

It is now necessary to consider the case of the propagation of the probe beam through a sample which exhibits a refractive index with a value n greater than one. If we denote as λ_0 the wavelength of the probe beam in air (strictly speaking in vacuum), then the wavelength of the field inside the sample will be,

$$\lambda=\frac{\lambda_0}{n}. \tag{2.40}$$

In Fig. 2.10 a function $f(x)$ at plane x propagates a distance z_1 in air to the plane x_1, then it propagates a distance z_2 through a medium with refractive index n up to the plane x_2. Finally it propagates a distance z_3 in air up to the plane x_3.

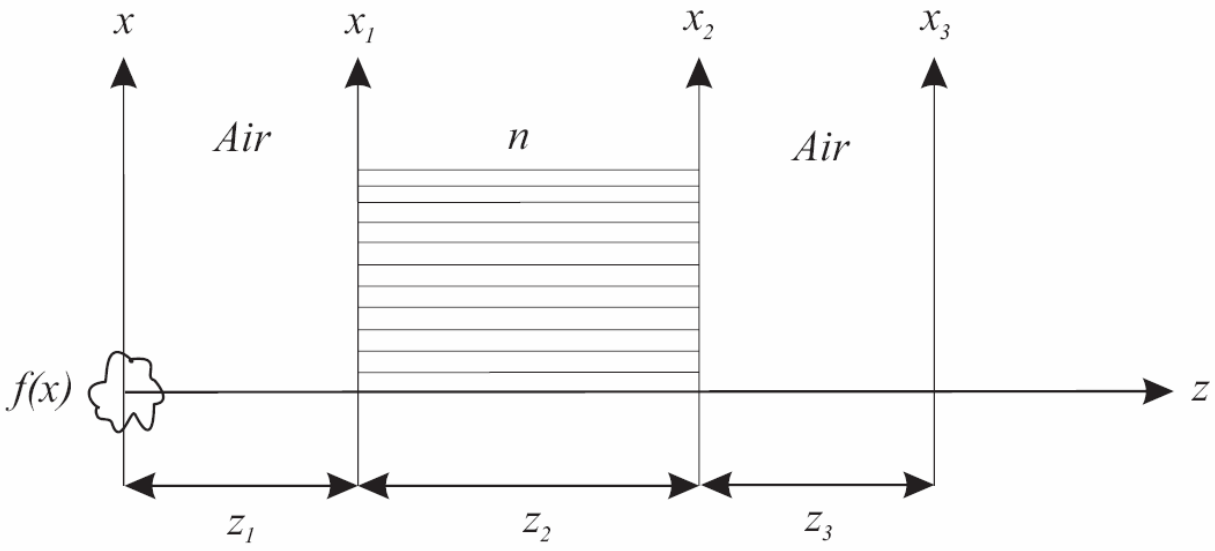

Fig. 2.10. Graphic description of the probe beam propagating from the object plane up to the image plane through a medium with refractive index greater than one.

For the situation depicted in Fig. 2.10 the integral in Eq. (2.39) is expressed as,

$$\int f(x)\exp\left[i\frac{\pi}{\lambda\left(z_1+z_2+\frac{z_3}{n_1}+\frac{z_4}{n_2}\right)}(x-x_4)^2\right]dx. \tag{2.41a}$$

Eq. (2.41a) is by itself of the outmost importance for revealing the essence of the technique. It clearly indicates that the Fresnel integral involves an overall distance of $\left(z_1+\frac{z_2}{n}+z_3\right)$. Being $\left(\frac{z_2}{n}\right)$ a distance that is virtually less than z_2 because the refractive index is grater than one.

By considering a virtual object with the same geometrical thickness as the object depicted in Fig. 2.10, and refractive index equal to one, one would obtain the following equation,

$$\int f(x)\exp\left[i\frac{\pi}{\lambda\left(z_1+z_2+z_3\right)}(x-x_3)^2\right]dx. \tag{2.41b}$$

Comparing Eqs. (2.41a) with (2.41b) it becomes apparent the survey of the technique. The probe beam travels from the object plane towards the image plane trough the sample. If the sample under test is a virtual one, the refractive index has a value of one. In contrast, when the sample is a real one, the refractive index is greater than one and the overall distance traveled by the probe beam results in a shorter apparent distance as compared with the virtual case. In consequence, the semi-width of the probe beam exhibits a change and this change is precisely the main key that allows us to determine the parameters of the sample under test. This result is described later in a following section.

Now it is convenient to describe our homodyne detector which is used to perform the measurements to characterize the parameters of the transmitted Gaussian beam.

Chapter 3

The homodyne detector

In this chapter we describe the knife-edge detector (ked), our experimental device used to perform the measurements to characterize the parameters of the transmitted Gaussian beam.

Before beginning with the description of the ked, we want to remark some of its features which we consider as advantages. As the ked is a non-invasive system, it has potential applications in areas like medicine and biology; it works at low power, this avoids damaging the sample under test and other optical components; it can be considered as a monochromatic system because it has a narrow emission band, and finally, due that the system has a continuous operation mode it is possible to model a linear and invariant system.

3.1 Setup for profilometry

The ked was originally intended for high-quality profilometry measurements and several important results were obtained and published [26]. Fig. 3.1 depicts one original-configuration setup for the ked.

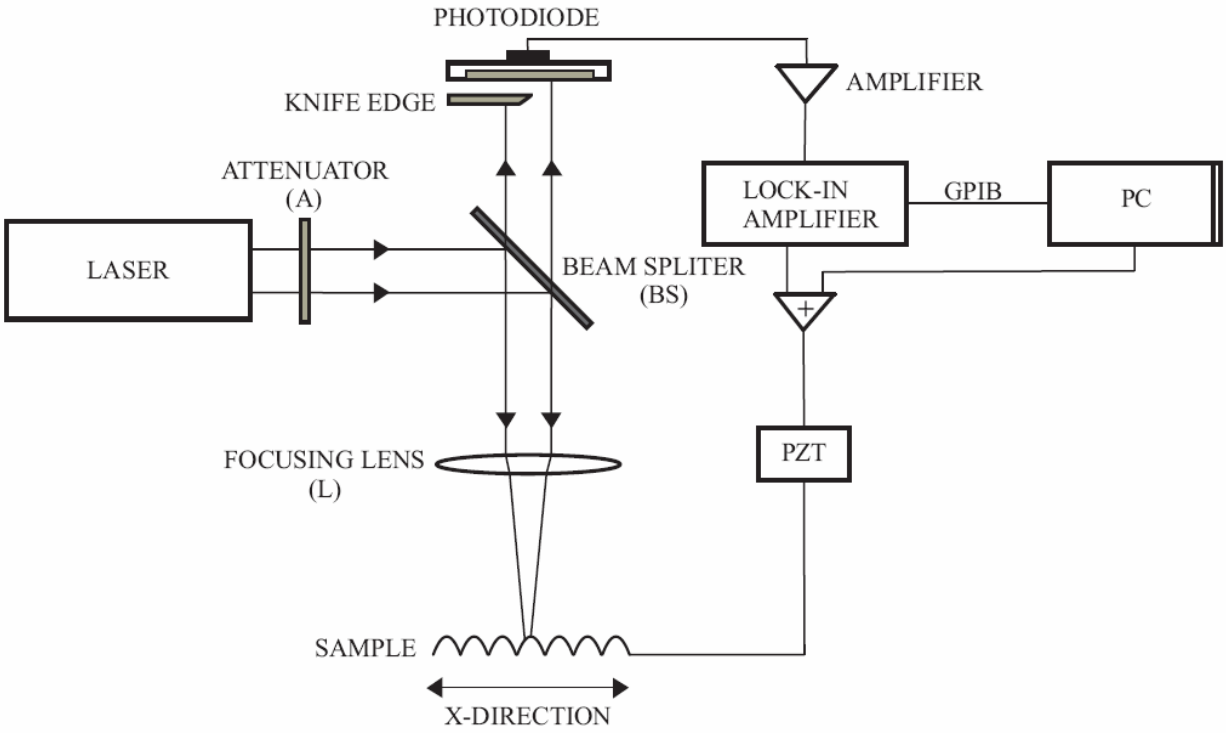

Fig. 3.1. Setup of the knife-edge detector for profilometry measurements. The elements depicted are described in the text.

In Fig. 3.1 an He-Ne laser (with wave-length λ equal to 632.8 nm) is focused on a sample under test by means of a focusing lens (L). A beam splitter (BS) is used to align the sample and a photo diode at different positions. The light reflected by the sample is collected by the photo diode. The photo diode whose sensitive area is much larger than the dimensions of the incoming beam is positioned behind a knife-edge. The knife-edge allows detecting variations in the signal due to the sample profile, in this manner obtaining an AC signal. If the knife-edge were not placed, a constant DC level would be obtained regardless of the sample shape. The sample is fixed to a flexure piezoelectric transducer (PZT) which has two purposes. First, it is used to displace vertically in plane the sample, in this way performing the scanning of the sample under test. Secondly, the PZT is used to vibrate the sample in a plane transversal to the optical axis at a low frequency (f) with small amplitude (δ_0). A flexure type PZT is preferred as it exhibits low tilt of less than 5 μrad. Finally the power collected by the photo diode is sent to an acquisition system. An attenuator (A)

is included to avoid damaging the optical components due to excessive heating.

3.2 Setup for measuring the illumination source profile

By introducing slight variations on the original setup, intended to widen its range of applicability, it was possible to measure small changes in the glucose concentration of transparent and turbid solutions. In this manner a theoretical characterization of the refractive index as a function of the glucose concentration was made for the first time to the best of our knowledge [27]. In addition, in this work we devised another setup which allows us to characterize the refractive index and geometrical thickness of optical samples. This homodyne detector setup is depicted in Fig. 3.2.

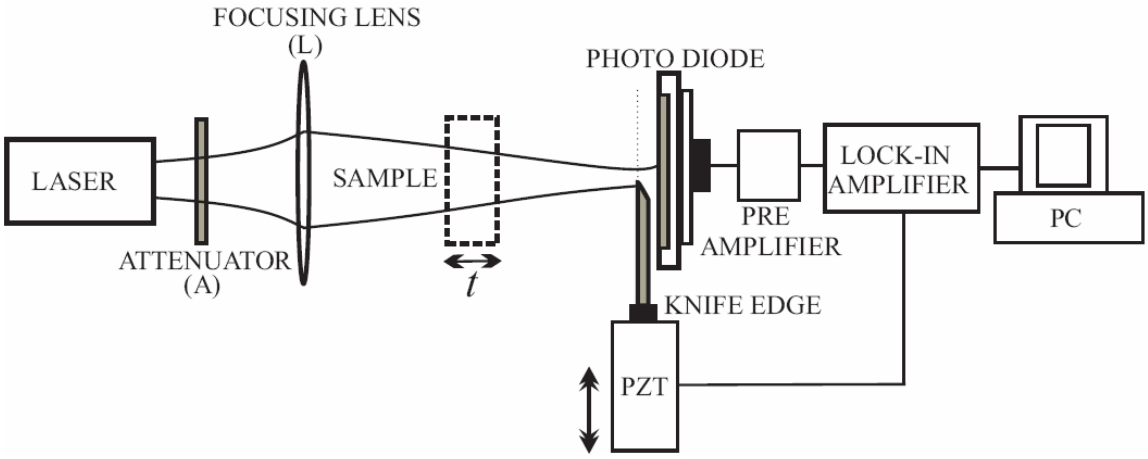

Fig. 3.2. Homodyne detector setup for measuring the parameters of the transmitted Gaussian beam.

Most of the elements depicted are the same described in Fig. 3.1, however some differences exist:

1. In this configuration it is not necessary to use a beam splitter because the system works in transmission mode instead of the original reflective mode.

2. Besides, for the purpose of including the sample under test between the lens and the knife-edge, we use a long working distance ($1\,cm$) lens, consisting in a Mitutoyo which focuses the beam at a semi-width of 1 micron.
3. In this configuration the knife-edge is attached to the PZT to perform a scanning of the probe beam, while in the original setup the scanning was performed on the sample, typically a calibrated reflective grating, and the knife-edge remained fixed.

Finally we want to remark that as we mentioned previously, our setup is non interferometric and this feature makes it suitable for measuring the thin pellicles discussed in the introduction section.

Now that we have described the optical part in the homodyne detector, it is convenient to provide the description of the acquisition system.

The signal collected by the photo-diode is sent to a pre-amplifier which amplifies the signal by changing the gain of the system with a variable internal resistance. The user can vary this gain to obtain the best possible signal, typically a signal with higher amplitude is preferable as it is dominant over the electronic noise. However there is a point where the system gets saturated, in this manner the user needs to calibrate the gain for every measurement depending on the illuminating power. The output signal is send to the lock-in amplifier. As mentioned, the lock-in vibrates the PZT at a unique frequency with a sinusoidal oscillation. In this manner the lock-in is capable of detecting an AC signal with a signal-to-noise ratio of 1000:1. The user can control this frequency which is usually as low as 20 hertz or less. Besides, the lock-in communicates with the PC via GPIB for sending data.

The output of the pre-amplifier can be also sent to a digital oscilloscope to verify in real time the measurements performed and parameters of interest of the signal like amplitude, frequency, shape, etc.

On the PC a ramp function is programmed and sent it via a DAQ card. This ramp allows to perform the scanning. Both signals, the sinusoidal oscillation and the ramp are the inputs of an adder circuit. The output is send to the PZT.

In this manner, the PZT is vibrating in an initial position; after a certain time it moves to a new position and continues vibrating and repeats the process until the whole scanning has been performed. This situation is depicted in Fig. 3.3.

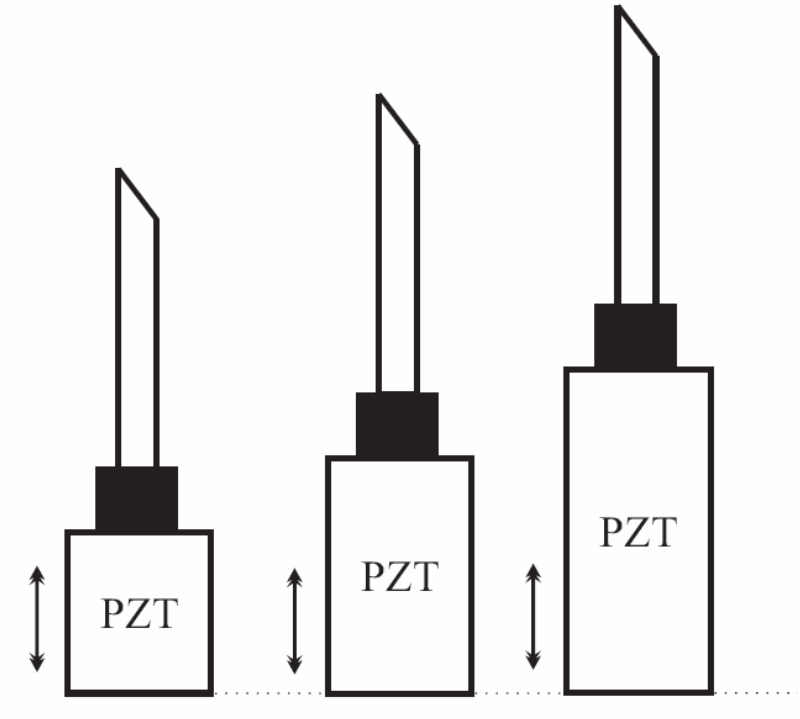

Fig. 3.3. Combined movement of the PZT. The PZT is vibrating at a low frequency and simultaneously it is expanding vertically, consequently displacing the knife-edge for the scanning. The expansion in the figure has been exaggerated for clarity.

As mentioned the frequency at which the PZT oscillates is controlled by the lock-in. This frequency is set low to avoid undesired movements of the knife-edge. The time that the PZT stays in a certain position is controlled by the PC. On the acquisition program the user controls this time called delay. The delay is set in milliseconds and in our experiments we have verified that a delay of 150 ms is suitable for our purposes. If the delay is set too slow, it is possible that the lock-in can not obtain a good average on the value of the signal amplitude at a certain point and erroneous measurements may be obtained.

Another parameter which is controlled on the display of the program is the number of pixels to be used. By increasing the number of pixels the PZT will scan a larger distance. An illustrative example of this situation is depicted in Fig. 3.4. In this example we simulate a scanning of a calibrated reflective grating with pitch 300 lines/mm. In 3.4a we set the system to 100 pixels to record two maxima of the grating. In 3.4b we double the number of pixels and consequently the distance we scan on the grating is double, recording four maxima.

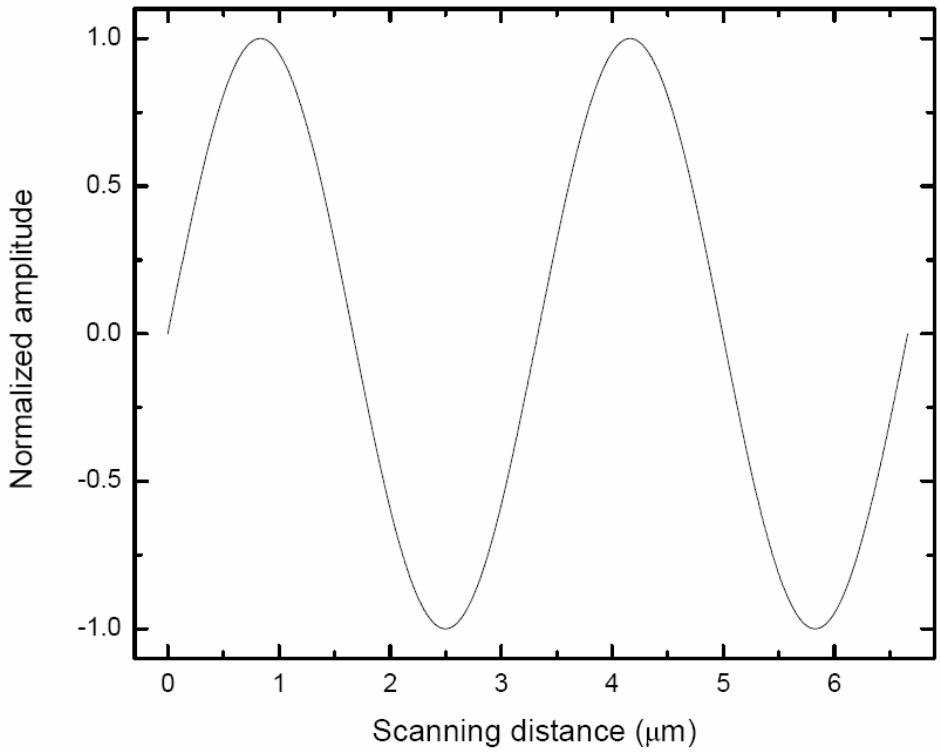

Fig. 3.4a. Simulation of a record of a calibrated grating with pitch 300 lines/mm obtained with 100 pixels.

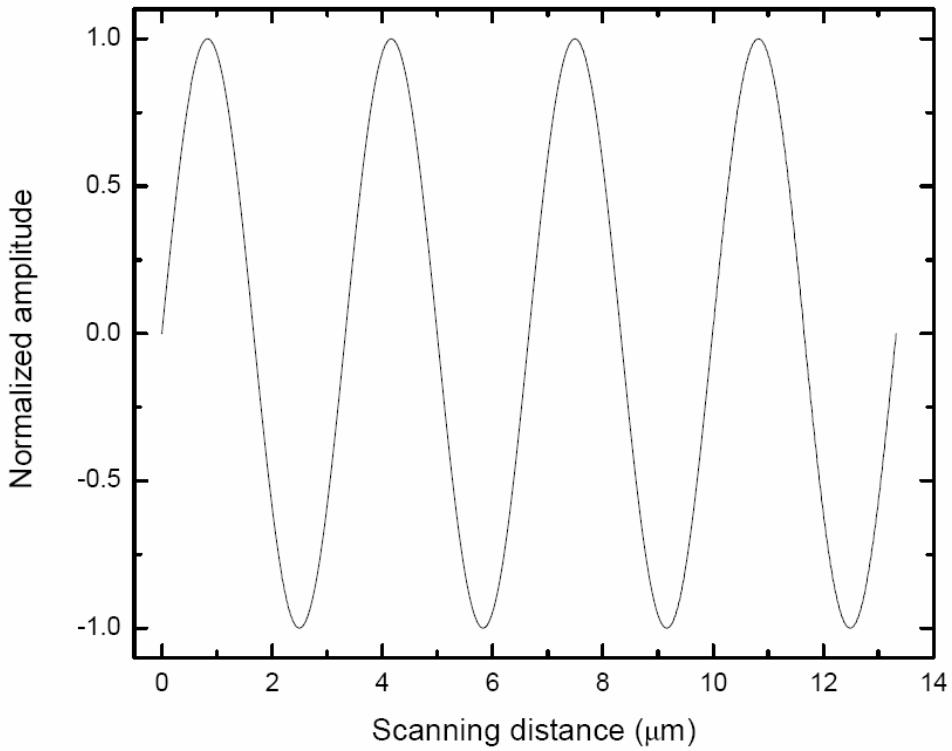

Fig. 3.4b. Simulation of a record of the calibrated grating depicted in Fig. 3.7a by using 200 pixels.

In the experiments the PZT is not completely linear as illustrated in the simulation of Fig. 3.4 but its behavior can be assumed that way with high precision for our purposes.

It is also important to remark that the PZT has a limit of expansion of about 100 microns. Therefore care must be taken to not exceed this limit with the number of pixels because the PZT can be damaged.

Finally, the combination of the delay with the number of pixels used to perform the measurements results in a scanning time. Each pixel is a position for the PZT and the delay is the time it will stay at that position. These parameters can be varied depending on the purposes of each measurement.

Now that all the elements of the homodyne detector have been described, we will provide an analytical expression for the power collected by the photodiode for two cases: with the presence of the knife-edge and without it.

3.3 The power collected

In Eq. (2.23) we provided the one dimensional amplitude distribution of the Gaussian beam. If its corresponding intensity distribution is to be obtained, it is necessary to multiply Eq. (2.23) by its complex conjugate. In this manner the expression in Eq. (2.28) is obtained, just by changing the axis ξ for x. It can be seen that the same is valid if Eq. (2.30) is used, because the imaginary exponential vanishes when the product is performed. Now we are interested in the optical power collected by the photodiode. For this let us consider the two dimensional case in which there is no knife-edge in front of the photo diode, thus all the incoming power impinges on it. The analytical expression for this situation is given by,

$$P = \int_{-\infty}^{\infty}\int_{-\infty}^{\infty} A^2 \exp\left[-\left(2\frac{x^2+y^2}{r_0^2}\right)\right]dxdy. \tag{3.1}$$

The expression in Eq. (3.1) can be divided in two separate integrals, and with a change of variable it follows that,

$$P = A^2\frac{r_0^2}{2}\int_{-\infty}^{\infty}\exp\left(-u^2\right)du\int_{-\infty}^{\infty}\exp\left(-v^2\right)dv. \tag{3.2}$$

The integrals in Eq. (3.2) are well-known. Therefore it can be noticed that the power is a constant on a certain plane, because the semi-width at that plane is fixed. As a consequence we will write the power as P_0 to denote that it is constant,

$$P_0 = \frac{\pi A^2 r_0^2}{2}. \tag{3.3}$$

It is possible to obtain an expression for A as,

$$A = \sqrt{\frac{2P_0}{\pi r_0^2}}. \tag{3.4}$$

By using Eq. (3.4) we can write the Gaussian amplitude distribution as,

$$\Psi(x,y) = \sqrt{\frac{2P_0}{\pi r_0^2}} \exp\left[-\frac{\left(x^2 + y^2\right)}{r_0^2} \right]. \tag{3.5}$$

Now we are going to obtain an expression for the optical power when the knife-edge is included. This situation is depicted in Fig. 3.5.

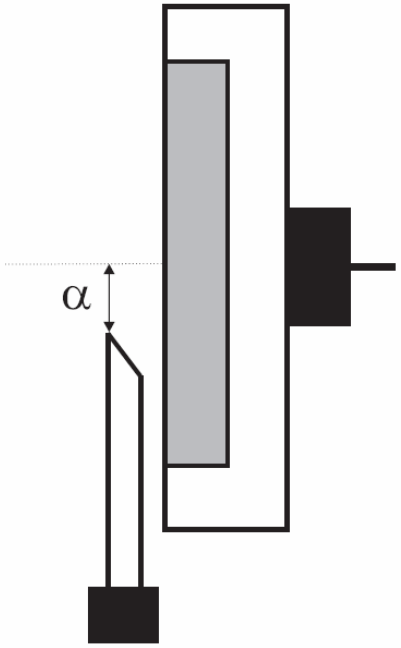

Fig. 3.5. Closer view of the knife-edge adjustment. It is desirable that the knife-edge covers half of the sensitive area of the photodiode. However, we include a possible adjustment error α which has been exaggerated for illustrative purposes.

Under the situation depicted in Fig. 3.5 the optical power collected by the photodiode can be written as,

$$P = \frac{2P_0}{\pi r_0^2} \int_{-\infty}^{\infty} \int_{\alpha}^{\infty} \exp\left[-\left(2\frac{x^2 + y^2}{r_0^2} \right) \right] dx\, dy. \tag{3.6}$$

In Eq. (3.6) the lower limit of one of the integrals changes because of the positioning of the knife-edge. It is not necessary equal to zero, corresponding to block exactly half of the beam, because a possible alignment error α, as depicted in Fig. 3.5. For this case it is also possible to solve two separate integrals. One of them can be solved in the same way as it was done in Eq. (3.2) obtaining,

$$P = \frac{2P_0}{\pi r_0^2} \sqrt{\frac{\pi}{2}} r_0 \int_{\alpha}^{\infty} \exp\left(-2\frac{x^2}{r_0^2} \right) dx. \tag{3.7}$$

Finally the optical power is given by,

$$P = \frac{P_0}{2} \, erfc\left(\frac{\sqrt{2}\alpha}{r_0} \right), \tag{3.8}$$

where for writing Eq. (3.8) the definition of the complementary error function, denoted $erfc(x)$ was used as follows,

$$erfc(x) = \frac{2}{\sqrt{\pi}} \int_{x}^{\infty} \exp\left(-t^2 \right) dt. \tag{3.9}$$

It is also convenient to provide the definition of the error function, denoted $erf(x)$ as,

$$erf(x) = \frac{2}{\sqrt{\pi}} \int_{0}^{x} \exp\left(-t^2 \right) dt. \tag{3.10}$$

Fig. 3.6 depicts a plot of the $erf(x)$, and Fig. 3.7 depicts the corresponding plot of the $erfc(x)$.

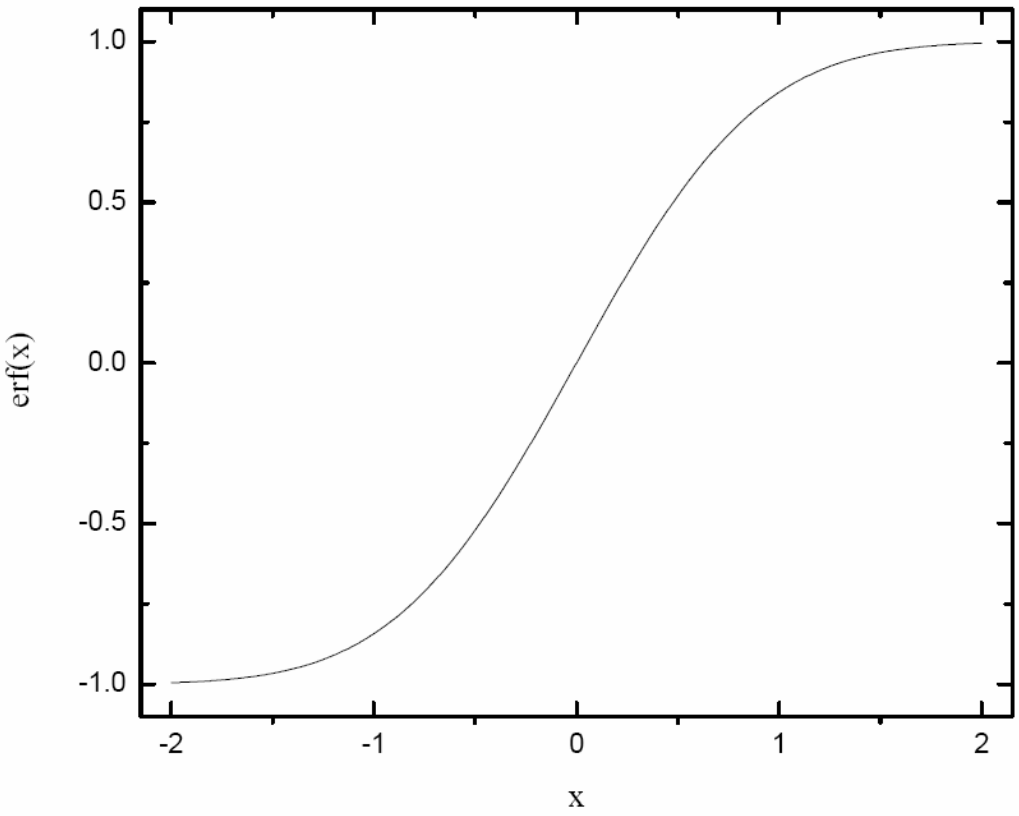

Fig. 3.6. Plot of the error function.

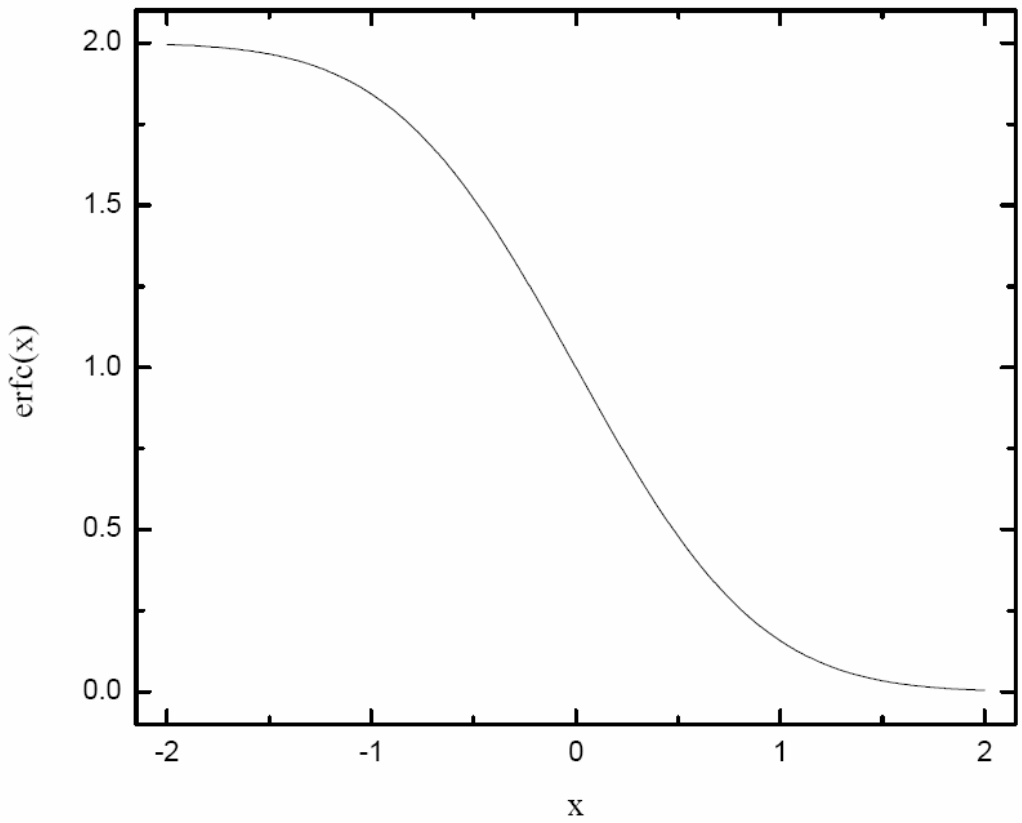

Fig. 3.7. Plot of the complementary error function.

As one of the main functions of the homodyne detector will be determining changes in the beam semi-width when the sample is included in the setup, we describe this process in the following section.

3.4 Measuring the beam semi-width

Measuring changes in the beam semi-width with accuracy is important for the measurements required for the adequate characterization of the optical media. These changes can be due to a variation on the concentration of a solution under test or, in our case, due to a sample tilt at different angles. In this sense, the vibrating knife-edge allows determining the semi-width of the Gaussian beam in a homodyne way as follows.

First consider the case when the knife-edge is not vibrating, due to the photodiode large sensitive area, the power collected (P) can be written as,

$$P = A\int_{\alpha}^{\infty} \exp\left(-2\frac{x^2}{r_0^2}\right)dx. \tag{3.11}$$

In Eq. (3.11) A is a constant scale factor and the lower limit of the integral (α) represents the initial position of the knife-edge. r_0 is the semi-width of the beam at the plane of detection. In summary, Eq. (3.11) establishes that the photodiode integrates the overall beam excluding the portion covered by the knife-edge.

Now, when the knife-edge is vibrating, the lower limit is written as,

$$\alpha = x_0 + \delta_0 \cos(2\pi f t), \tag{3.12}$$

where x_0 is a static position of the vibrating knife-edge. By substituting Eq. (3.12) in Eq. (3.11) and by performing an expansion in power series of the resulting equation, the linear term is of the form,

$$P_{linear}(x_0) = B\exp\left(-2\frac{x_0^{\,2}}{r_0^{\,2}}\right)\cos(2\pi f t), \tag{3.13}$$

where B is a constant. The expansion is performed only to the first term as the lock-in amplifier is tuned to the first harmonic. Thus, the signal results proportional to the intensity Gaussian profile evaluated at x_0 as indicated by Eq. (3.13).

To accurately obtain the overall shape of the Gaussian beam with our homodyne detector it is necessary to displace the position of the knife-edge to different values of x_0. In this way, the shape and width of the Gaussian beam are obtained with high accuracy at the plane of detection.

As the lock-in is tuned to the first harmonic, the signal results proportional to the intensity Gaussian profile evaluated at x_0 as indicated by Eq. (3.13). To obtain the overall profile the knife-edge is displaced in plane to different x_0

positions. In Fig. 3.8 we provide an example where plots of Gaussian distributions obtained experimentally are shown: the solid line represents the profile measured without the sample and the dashed line is the case when the sample is included in the setup.

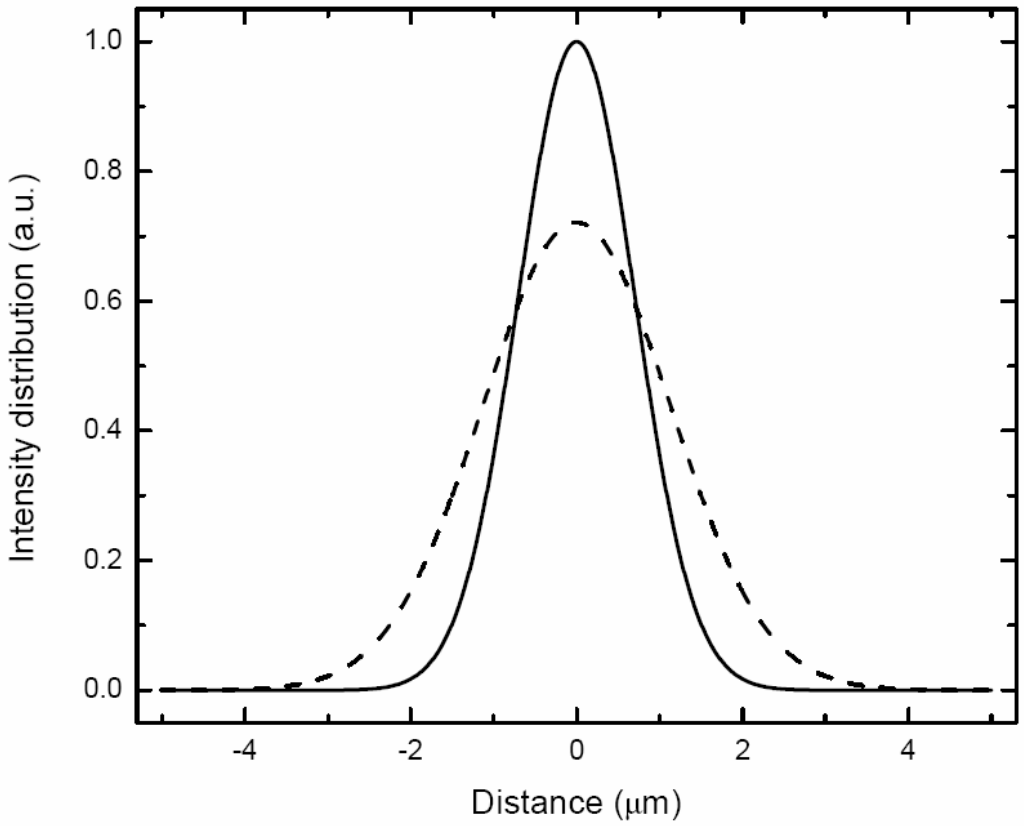

Fig. 3.8. Gaussian intensity distributions obtained experimentally without the sample (solid line) and with the sample included (dashed line).

It can be seen that in the absence of the sample the amplitude is higher and the semi-width is thinner and with the sample included occurs the opposite, the amplitude decreases and the semi-width increases. This is because the area under the curve, the power, is constant.

At this point our analytical tools and our experimental setup have been described and we are ready to provide the methodology used for the characterization of the pellicle in air.

Chapter 4

Characterization of the pellicle in air

Our proposal for the determination of the refractive index and the geometrical thickness of a thin pellicle in air is as follows.

Let us consider a laser beam which is focused at the plane of observation with coordinates (ξ,η) at the absence of the sample, by means of a focusing lens placed on a coordinate plane (x_1, y_1) at a distance z_0 from the laser output. This is depicted in Fig. 4.1.

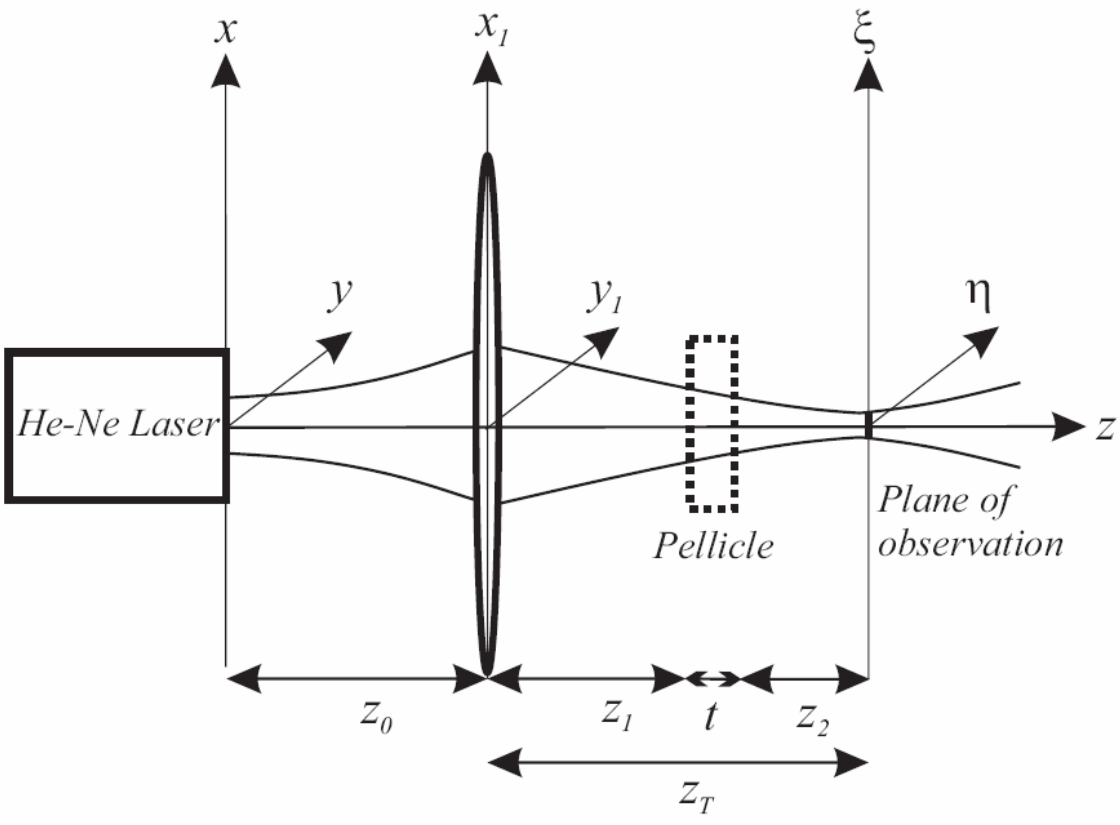

Fig. 4.1. Propagation of the Gaussian beam as described in the text. z_T is set such that the plane (ξ,η) corresponds to the best focusing plane.

The lens is considered very thin and its aperture is large enough to allow neglecting truncation of the beam. The plane of observation is adjusted at a

distance z_T behind the lens to attain the best focusing conditions (minimum beam semi-width). We will refer to this plane as the best focusing plane. Once z_T has been fixed, the pellicle to be characterized, which has a geometrical thickness t, it is introduced transversally to the optical axis z in the optical path. It can be seen that,

$$z_T = z_1 + t + z_2 , \tag{4.1}$$

where z_1 and z_2 are depicted in Fig. 4.1. These distances can be chosen arbitrarily as it will be demonstrated below. For illustrative purposes the width of the sample has been exaggerated in Fig. 4.1. The overall propagation of the Gaussian beam through the system can be calculated by means of the Fresnel integral. We first consider a virtual sample, that is, a sample with a refractive index equal to one and geometrical thickness t. For this condition we calculate the overall propagation from the laser up to the plane of observation and we plot the semi-width of the Gaussian beam as a function of distance z_T. These calculations allow characterizing all the parameters involved in the propagation of the beam.

There is a value of z_T in which the semi-width exhibits a minimum at the plane of observation; this z_T value will be referred as the best focusing distance and the corresponding transversal plane will be the best focusing plane. As mentioned, for a full characterization of the beam propagation, it is necessary to calculate the overall propagation from the laser output up to the plane of observation. For simplicity in the description of our proposal this is not necessary; it is sufficient to begin our description by considering the beam distribution just after the lens, as the case treated in chapter 2, Eq. (2.30). For this distribution we obtain at the plane of observation the corresponding semi-width, denoted (r_A), in a similar way as it was done in Eq. (2.33), for convenience it is repeated here as,

$$r_A = \frac{\sqrt{\lambda^2 z_T{}^2 + r^4 (\beta \lambda z_T - \pi)^2}}{\pi r}. \tag{4.2}$$

We emphasize that Eq. (4.2) corresponds to the case of a virtual sample with a refractive index equal to one. r_A, r, β and λ are determined experimentally by the homodyne detector. In this manner we propose a value for z_T which matches with our experimental conditions and it is unique.

By maintaining z_T constant we now repeat the same calculation for a pellicle with a refractive index n and geometrical thickness t. By using a similar treatment as in Eq. (2.41a) the semi-width r_B is given as,

$$r_B = \frac{\sqrt{\lambda^2 \left(z_1 + \frac{t}{n} + z_2 \right)^2 + r^4 \left[\beta \lambda \left(z_1 + \frac{t}{n} + z_2 \right) - \pi \right]^2}}{\pi r}. \tag{4.3}$$

In writing Eq. (4.3) it has to be noticed that multiple reflections on the boundary do not affect the semi-width of the transmitted amplitude, as is typical when using pellicle beam splitters. On the contrary, the transmitted amplitude is drastically affected by multiple reflections. Because r, β and λ are fixed, it will be noticed from Eq. (4.3) that exactly the same value of r_B can be obtained with an uncountable set of samples, as follows,

$$z_1 + \frac{t}{n} + z_2 = z_1' + \frac{t'}{n'} + z_2' = z_1'' + \frac{t''}{n''} + z_2'' = \cdots, \tag{4.4}$$

where the primed values stands for the set of possible samples. Fig. 4.2 shows an illustrative example to clarify the above mentioned. Two different samples, denoted sample 1 and sample 2 produce the same semi-width at the best focusing plane. Sample 1 has thickness t and refractive index n while sample 2 has thickness t' and refractive index n'.

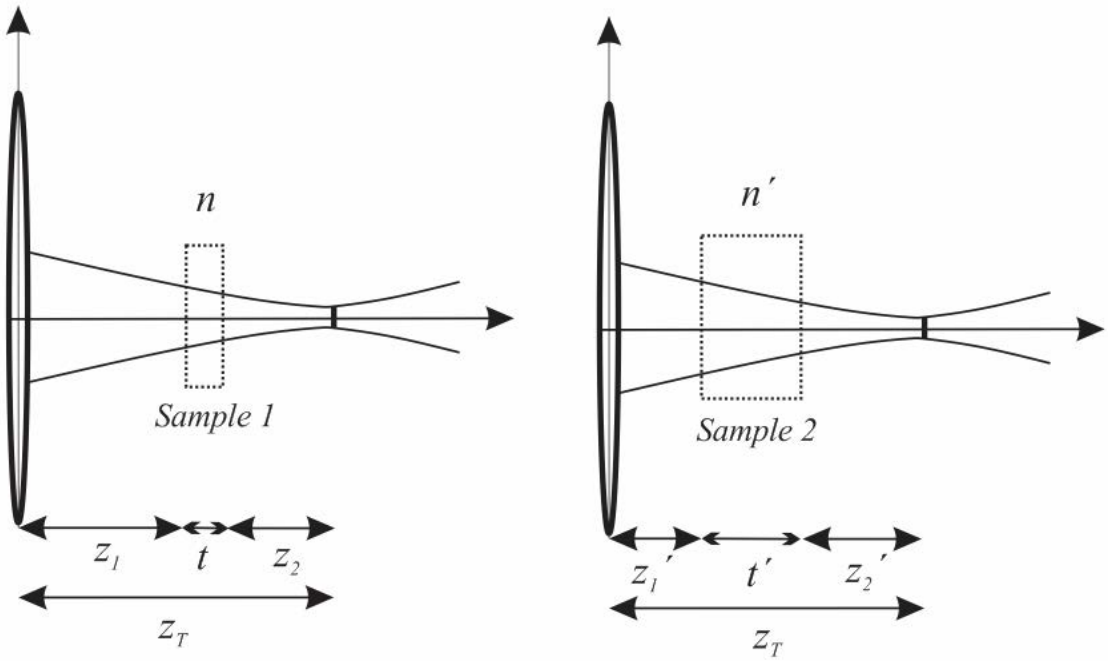

Fig. 4.2. Descriptive example where two different samples produce the same beam semi-width at the best focusing plane. Sample 1 has thickness t and refractive index n while sample 2 has thickness t' and refractive index n'. The remaining parameters are described in the text.

As it can be seen from Fig. 4.2 it is only necessary that z_T remains fixed to attain the same semi-width for both cases. The separation between the sample and the lens, denoted z_1 does not affect this parameter, the same occurs for z_2. Because of that we say that the system is immune to vibrations of the pellicle along the z axis. This feature is of the utmost importance as it overcomes the main disadvantage of the interferometric techniques when it is intended to measure a very thin and unsupported sample.

From Eq. (4.1) we can write,

$$z_1 + z_2 = z_T - t, \tag{4.5a}$$

or by considering the second sample case,

$$z_1' + z_2' = z_T - t'. \tag{4.5b}$$

By substituting Eqs (4.5) in Eq. (4.4) we obtain,

$$z_T - t + \frac{t}{n} = z_T - t' + \frac{t'}{n'}, \tag{4.6}$$

which can be expressed as,

$$t\left(\frac{1}{n} - 1\right) = t'\left(\frac{1}{n'} - 1\right). \tag{4.7}$$

In this manner, we can generalize the result obtained in Eq. (4.7) for multiple samples as follows,

$$t\frac{n-1}{n} = t'\frac{n'-1}{n'} = t''\frac{n''-1}{n''} = \cdots \tag{4.8}$$

Eq. (4.8) shows that the geometrical thickness multiplied by the ratio of the refractive index diminished in one divided by the refractive index is an invariant, provided z_T remains constant, which in our case corresponds to the best focusing plane. As mentioned, it is important to remark that the semi-width at the best focusing plane is independent of the position of the sample, that is, independent of the actual values of z_1 and z_2. Thus back and forth movements of the plate under inspection do not affect the size of the Gaussian beam under measurement. An invariant factor F can be defined as,

$$F = t\frac{n-1}{n}. \tag{4.9}$$

Eq. (4.9) is one of the keys in the calculations of the refractive index and geometrical thickness of our proposal.

Fig. 4.3 depicts an illustrative example where three different samples produce the same semi-width. Fig. 4.3a depicts a sample with the following parameters: $n=1.5$ and $t=10\mu m$. By means of Eq. (4.9) we obtain $F=3.33\mu m$. In our theoretical simulation by using this parameters we obtain a focused beam with semi-width $r_B=1.16\mu m$.

Fig. 4.3b depicts a sample with the same value of F as requested by Eq. (4.8), however in this case the refractive index increases and its corresponding geometrical thickness decreases maintaining the same value for F and as a consequence obtaining the same Gaussian semi-width. The numerical values obtained for n and t are shown in the figure.

Finally in Fig. 4.3c n decreases while t increases accordingly and r_B is also obtained. The numerical values are also included in the figure.

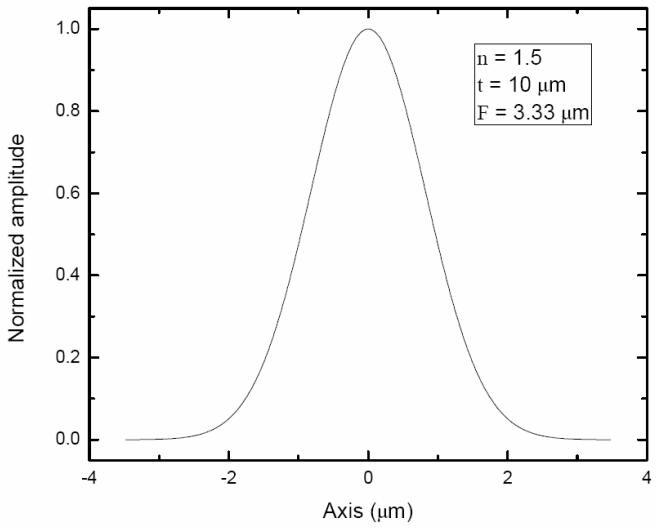

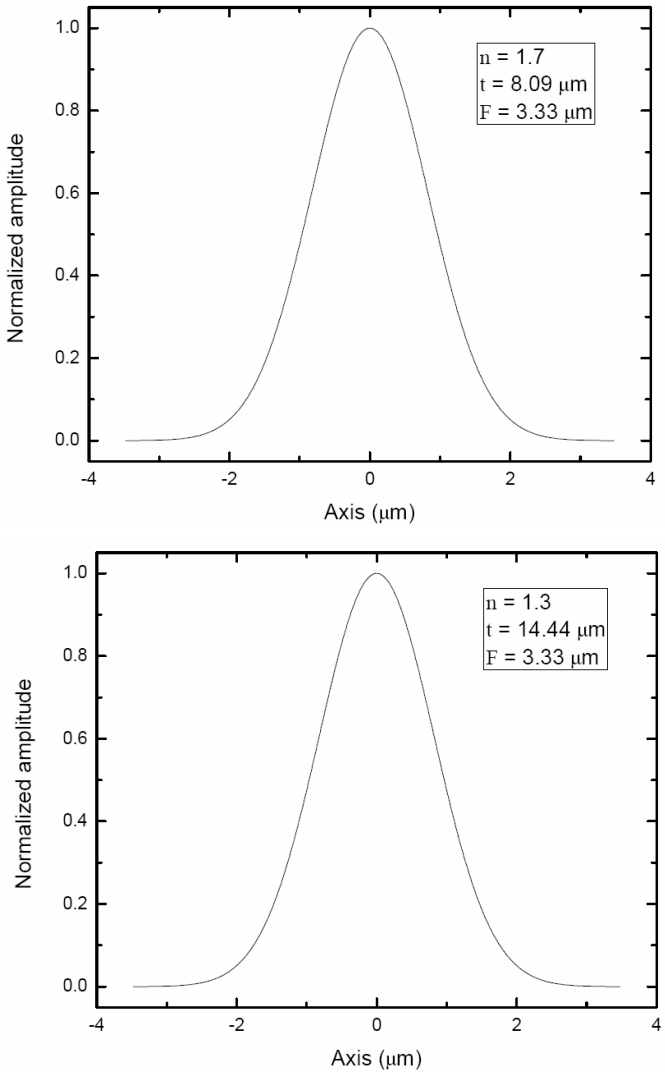

Fig. 4.3. Comparison of three different samples which produce the same Gaussian semi-width at the focusing plane. The parameters are: a) $n = 1.5$ and $t = 10\mu m$; b) $n = 1.7$ and $t = 8.09\mu m$; c) $n = 1.3$ and $t = 14.44\mu m$. For the three cases $F = 3.33\mu m$ and $r_B = 1.16\mu m$.

From Eq. (4.3) it can be noticed that the value of t/n can be calculated by knowing r_B. However n and t can not be calculated independently.

To overcome the problem mentioned above, we additionally use the equation of the power (P) transmitted by a pellicle in a homogeneous medium. This is a well known equation [28-29] and for convenience is repeated here as,

$$P = \left(\frac{4 n_0 n_1}{M} \right)^2 , \tag{4.10}$$

where n_0 and n_1 are the refractive indices of the homogeneous medium and the pellicle respectively and,

$$M = \begin{vmatrix} 1 & -1 & -1 & 0 \\ -n_0 & -n_1 & n_1 & 0 \\ 0 & \exp\left(-i \frac{2\pi}{\lambda} n_0 n_1 t \right) & \exp\left(i \frac{2\pi}{\lambda} n_0 n_1 t \right) & -1 \\ 0 & n_1 \exp\left(-i \frac{2\pi}{\lambda} n_0 n_1 t \right) & -n_1 \exp\left(-i \frac{2\pi}{\lambda} n_0 n_1 t \right) & -n_0 \end{vmatrix} . \tag{4.11}$$

Eqs (4.10) and (4.11) are valid for plane waves and are applied here with reasonable accuracy as the pellicle is preferable placed as close as possible to the focal plane, in the Rayleigh zone, where the wave is almost collimated.

Eqs. (4.10) and (4.11) will be combined with Eq. (4.9) to fulfill the information needed. For this, it is necessary to measure accurately the power of the Gaussian beam transmitted by the pellicle. Actually what we require is the ratio of the power detected when the pellicle is present divided by the power detected without the pellicle. In turn, to measure the power by integrating the intensity of the Gaussian profile, it is necessary to measure with good accuracy the semi-widths of the beams under detection. This is done by means of the homodyne detector which is immune to spurious light, harmonics and undesired DC components.

Before continuing with our description we want to remark that it is not necessary to actually measure the geometrical distances depicted in Fig. 4.1. Instead of this, we use the homodyne detector to characterize the overall experimental propagation of the Gaussian beam. Now, we use the theoretical setup of Fig. 4.1 which uses an ideal lens and we fix the corresponding parameters properly to match both propagations. As both propagations coincide everywhere, both the theoretical and the experimental propagations are the same. As a consequence, when a thin sample is introduced in the

focused beam, between the lens and the plane of detection, the theoretical model must also match with the experimental setup. In this way we have a model that allows us to determine the parameters of the sample under study.

In our experiments the intensity spot size without the pellicle at the best focusing plane was approximately 2 μm. As the pellicle physically had to be placed away of this plane, we estimate that the pellicle was illuminated by a beam with a spot size of about 20 μm. Thus, our measurements represent a local value over this region. The corresponding power is obtained by integrating the area under the Gaussian distribution.

As all the parameters in the experiment are maintained fixed, it is possible to obtain the relative power (P_{rel}) as the ratio between the power when the sample is placed (P_{film}), referenced to the power measured without the sample (P_{air}),

$$P_{rel} = \frac{P_{film}}{P_{air}}. \tag{4.12}$$

Eq. (4.12) represents one of the most important parameters of our proposal.

Once the semi-widths have been accurately measured with the homodyne detector, we proceed to assign to r_A and r_B in Eqs. (4.2) and (4.3) their corresponding values. The parameters r , β and z_T were previously characterized and calculated numerically by means of the overall diffraction propagation of the beam.

Next we propose arbitrary values to z_1 , z_2 and n to calculate its corresponding t value, taking care to fulfill with Eq. (4.1). In this manner, we have chosen one of the uncountable set of possibilities that match with our experimental semi-width. With these values we proceed in calculating the invariant factor F given by Eq. (4.9) and the relative transmitted power as given by Eq. (4.12).

At this point it will be noticed that Eq. (4.10) contains sinusoidal terms on n and t . This behavior is illustrated in Fig. 4.4 that shows a plot of the

transmitted power as a function of t calculated with the referred equation. In this plot the corresponding relative power obtained experimentally is also included and represented with a solid horizontal line. The values of t in the plot are obtained by varying n in a range between 1.5 and 1.9, while maintaining fixed F given by Eq. (4.9). In Fig. 4.4 circles correspond to the intersection of the continuous possible powers with the experimentally obtained relative power.

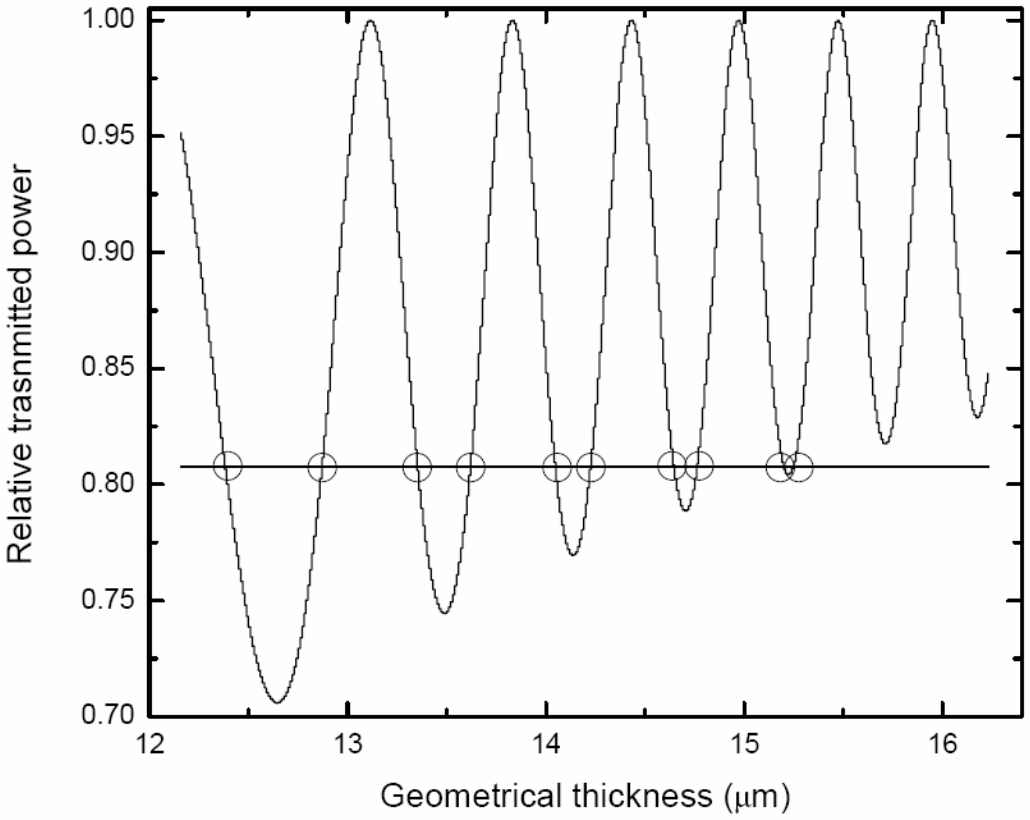

Fig. 4.4. Plot of the theoretical relative power transmitted by the sample as a function of its geometrical thickness obtained with Eq. (4.10) (oscillating plot). The horizontal line corresponds to the transmitted power measured experimentally. The circles represent the intersection of both plots (the allowable powers).

It will be noticed that the plot in Fig. 4.4 is not periodic. This is a result of substituting Eq. (4.9) in Eq. (4.10) with n substituted by n_1. As the only allowable values correspond to the intersection of both plots represented by

circles in Fig. 4.4, now, the set of possible geometrical thicknesses has been reduced to only ten possibilities. It is now necessary to discern which one corresponds to the sample, and with the data available it is not possible. As a consequence we have devised the following procedure.

We displace the sample slightly to measure in a neighbor spot. At this new position we measure again with the homodyne detector as it was done with the former measurement. For comparative purposes we repeat Fig. 4.4 in Fig. 4.5 where plots of the second measurement represented by dashed lines have been added. In Fig. 4.5 circles represent the ten possible values allowable for the first measurement and squares represent the allowable 14 possible values for the second measurement.

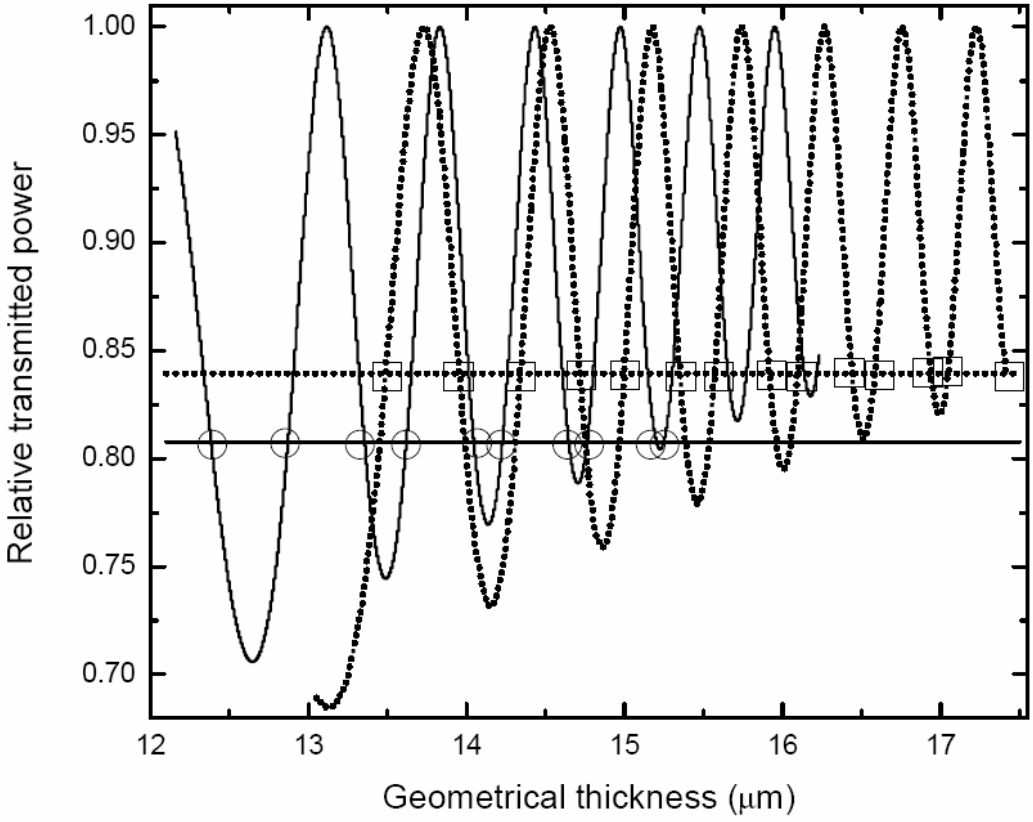

Fig. 4.5. Plots of the relative transmitted powers as a function of the geometrical thickness for two neighbor spots obtained with Eq. (4.10) in a similar way as Fig. 4.4. The horizontal lines correspond to the relative powers transmitted by the sample which are measured experimentally as described in

the text. Circles correspond to allowable values for the first measurement, squares for the second measurement.

At this point, we have calculated F for the first measurement and a corresponding F' for the second measurement. We have found a set of ten possible thicknesses for the first measurement and 14 for the second one. Now, being the refractive index a characteristic of the material composition, it should remain basically constant on the small vicinity where the measurements were performed. Thus,

$$F = t\frac{n-1}{n}, \tag{4.13a}$$

$$F' = t'\frac{n-1}{n}, \tag{4.13b}$$

for each measurement respectively which allow us to divide Eq. (4.13a) by Eq. (4.13b) to eliminate n as,

$$\frac{F}{F'} = \frac{t}{t'}. \tag{4.14}$$

As F and F' are known values, Eq. (4.14) implies that the ratio of the thicknesses is also known. To determine t and t' we take all the combinations that correspond to the 10 values of the first measurement against the 14 values of the second one until the ratio fits better. In this way all the non allowable values are discarded remaining only the pair t and t' which is the unique allowable solution. Finally by using Eqs. (4.13a) and (4.13b) two refractive indices are obtained, n and n'. These two values are expected to be the same but as they were obtained experimentally, an inherent small difference arises and it is considered in the error uncertainty.

To verify the correctness of the results we performed the same measurement on a third neighbor spot. Table 4.1 summarizes the results obtained.

Measurement	n_1	n_2	n_3	$t_1(\mu m)$	$t_2(\mu m)$	$t_3(\mu m)$	Δn
Spot1 - Spot2	1.758	1.757	-	13.35	14.34	-	$1x10^{-3}$
Spot2 - Spot3	-	1.757	1.752	-	14.34	14.83	$5 x10^{-3}$
Spot1 - Spot3	1.758	-	1.752	13.35	-	14.83	$6 x10^{-3}$

Table 4.1. Values obtained for the refractive index and geometrical thickness for each combination of the three measurements on the stretch film.

Table 4.1 lists the experimental results obtained with our proposal of measuring with pairs of neighbor spots. The results confirm the correctness of our technique as the results are consistent when measuring with different pairs. Obviously more spots can be taken to improve the trustworthiness of the technique. For illustrative purposes we have limited this report to only three.

Chapter 5
Characterization of the optical plate

Following our research, after the characterization of the pellicle in air, we noticed that a similar approach can be applied to characterize the refractive index and the geometrical thickness of a semi-transparent optical plate. Most of the theory described in the previous chapter is also valid for this case. The main differences were mentioned in the introduction section and are repeated here for clarity: We realize that no power measurements are required for characterizing the optical plate, as a consequence the sample does not need to be highly transparent. In this manner, with our technique we are able to characterize semi-transparent samples. Besides, for the case of the pellicle we used the equations of the power transmitted by a pellicle in a homogeneous medium. As the optical plate can not be treated as a pellicle due to its greater thickness, we measure the beam semi-width at normal incidence and we also measure the shift of the Gaussian centroid when the sample is tilted at different angles to determine both parameters of interest separately. The propagation of the Gaussian beam from the laser up to the detection plane is the same described in Chapter 4 for the pellicle case. The shift of the Gaussian centroid is as follows.

5.1 Shift of the Gaussian centroid

In Fig. 5.1 a beam impinges on an optical plate of thickness t and refractive index n with an angle θ with respect to the normal N as depicted. We assume that the end borders of the plate are parallels. As our technique measures in a very thin spot of a high quality sample, this assumption seems reasonable.

The oblique incidence will cause two effects: first, the beam will travel a larger distance inside the sample making the Gaussian beam wider at the plane of detection. It has to be remarked that this broadening of the beam is irrelevant

for our proposal as it is not necessary to measure the semi-width of the beam when the sample has been tilted; it is only necessary to measure the semi-width in the transversal case.

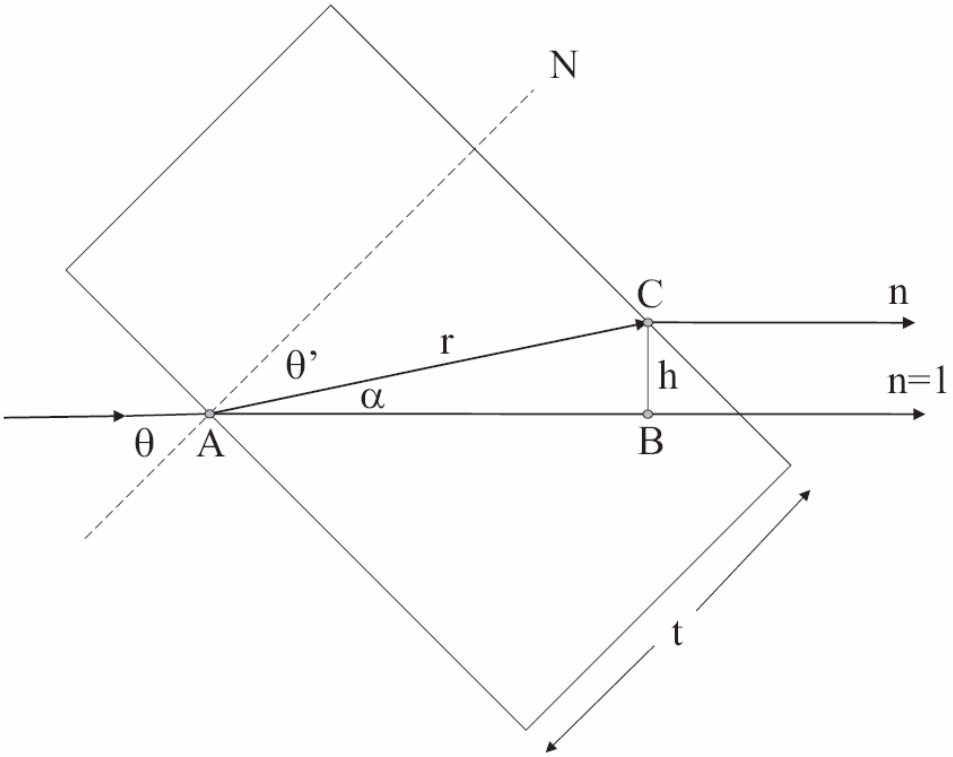

Fig. 5.1. Shifting of the beam centroid due to sample tilting.

The second effect caused by tilting the sample is a shift on the centroid at the plane of detection.

Let us assume that an incoming Gaussian beam impinges on a point A of a virtual glass plate (GP) of refractive index equal to one and thickness t. The incident beam forms an angle θ' with respect to the normal N as depicted in Fig. 5.1. As the beam stays in air it propagates up to the point B. Now we replace the virtual GP for a real one with refractive index n greater than one and the same thickness t. Because of the real GP the Gaussian beam is refracted and it propagates by a different path until it reaches the interface at point C. After C both beams will propagate in parallel paths. However the center of the Gaussian beam suffered a shift or displacement between the virtual and the real GP denoted by h. r and α are the distance and the angle showed in Fig 5.1, respectively. By simple geometry we have,

$$h = r\sin(\alpha), \tag{5.1}$$

and,

$$r = \frac{t}{\cos(\theta')}. \tag{5.2}$$

By using that $\alpha = \theta - \theta'$ and the Snell law the centroid shift h can be given as,

$$h = t\frac{\sin\theta\sqrt{n^2 - \sin^2\theta} - \sin\theta\cos\theta}{\sqrt{n^2 - \sin^2\theta}}. \tag{5.3}$$

Measuring the shift h and the beam semi-width at normal incidence allows using Eqs. (4.9) and (5.3) to calculate t and n. For convenience Eq. (4.9) is repeated here and numbered as Eq. (5.4),

$$F = t\frac{n-1}{n}. \tag{5.4}$$

Up to this point the bases of our proposal have been introduced. Before proceeding further it will be convenient to study the behavior of Eqs. (5.3) and (5.4) graphically. This is presented in the following section.

5.2 Theoretical behavior of the basic equations

By combining Eqs. (5.3) and (5.4), we obtain,

$$h = F\frac{n}{n-1}\frac{\sin\theta\sqrt{n^2 - \sin^2\theta} - \sin\theta\cos\theta}{\sqrt{n^2 - \sin^2\theta}}. \tag{5.5}$$

Experimentally measuring r_A, r_B and z_T allows us to determine values for n and t corresponding to the uncountable set of possible samples. Once fixed n and t, F is known. Additionally if t is maintained fixed, then, it is possible to use Eq. (5.5) to plot h as a function of θ. Fig. 5.2 depicts plots of h as a function of θ for an illustrative case of a sample with t = 140 μm and three different values of n: 1.4, 1.5 and 1.6.

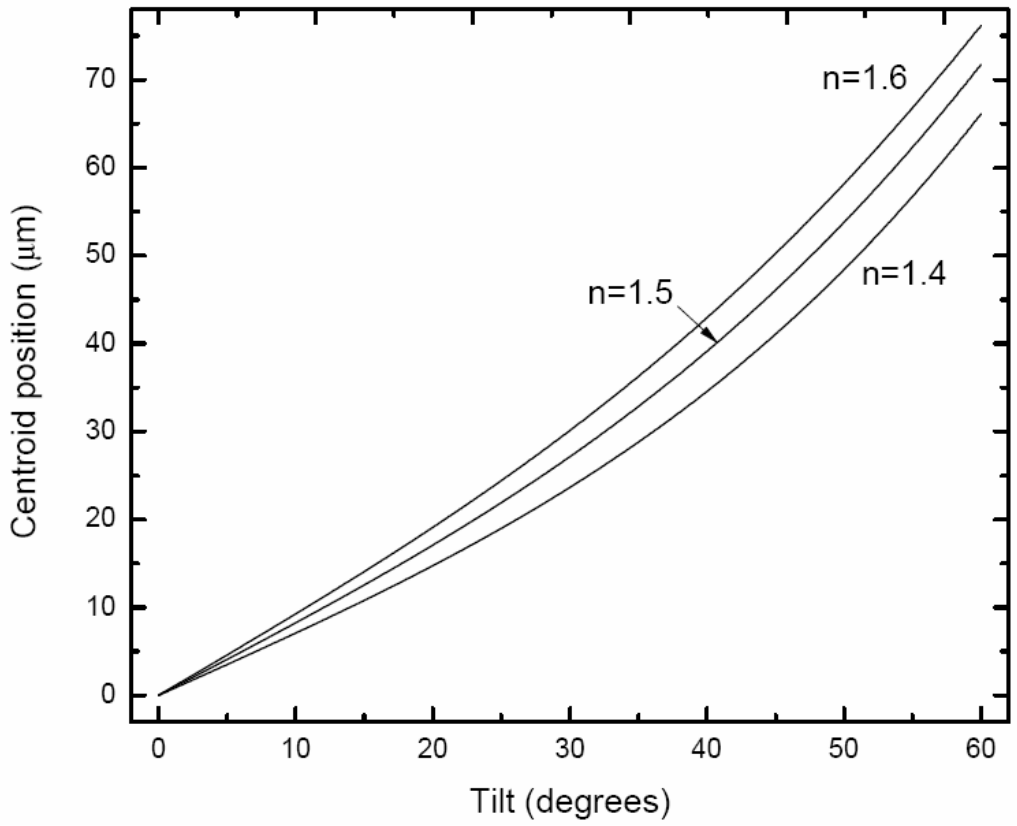

Fig. 5.2. Plots of the centroid position as a function of the tilt for three samples with t = 140 μm and $n = 1.4$, $n = 1.5$ and $n = 1.6$ respectively.

From Fig. 5.2 it can be noticed that as the tilt increases the separation between the curves is also increasing. This indicates that the system becomes more sensitive at higher tilts inside a useful region.

With a commercially available translation-stage we displace along the optical axes the homodyne detector and we recorded the Gaussian profile at different positions. The minimum semi-width obtained corresponds to the best

focusing conditions. At this plane the values of z_T and r_A are registered. In our experiment r_A is approximately one micron. If the detector is maintained at this plane the system will exhibit maximum sensitivity which is desirable for very thin samples. As in our case the expected geometrical thickness of the sample is in the range of 120-170 microns it is convenient to displace the homodyne detector slightly from the best focusing plane because our PZT has a maximum scanning distance of 100 microns. For our experimental purposes this displacement is about $4.5\mu m$. The other working conditions are: $\beta = 4.971\times10^{8} m^{-2}$, $r = 2.2mm$, $r_A = 1.4\mu m$, $z_T = 1.0cm$, $\lambda = 0.632\mu m$.

Next, the sample is placed at normal incidence (zero tilt). Its placement is easily done as its corresponding centroid has to coincide with the one of the profile recorded without the sample. Under this condition r_B is determined. In our case $r_B = 8.77\mu m$ which result in a value of $F = 44.45\mu m$.

Finally the sample is tilted in steps of 5 degrees up to 45 degrees by means of a precision rotary stage and the Gaussian profile is recorded for each case. Fig. 5.3 show plots of the profiles obtained. The plots are normalized with respect to the zero-tilt profile. For clarity Fig. 5.3 exhibits profiles obtained up to 30 degrees. The Gaussian profile measured without the sample is also included in the plot; its amplitude has been decreased about six times.

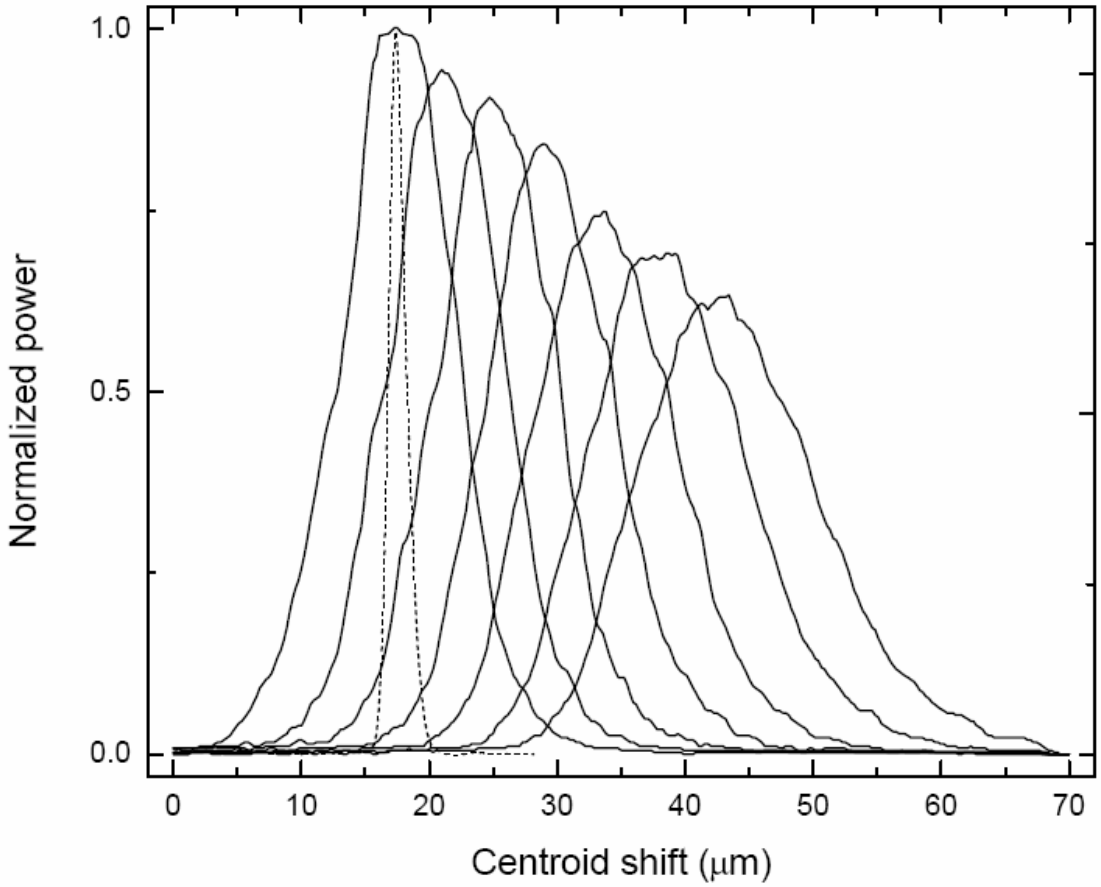

Fig. 5.3. Gaussian profiles measured with the homodyne detector. The narrowest profile (dashed line) is obtained without the sample and its amplitude is reduced approximately 6 times. The solid lines are the profiles measured with the sample tilted at different angles. The solid line profile at the left corresponds to the zero tilt case. The 30 degrees profile has the smaller vertical amplitude.

With the profiles recorded, a plot of the centroids as a function of tilt is performed. Fig. 5.4 depicts the experimental measurements (represented by circles) and the best fitted theoretical curve obtained with Eq. (5.5). The fitting curve is determined with a least square method. The optimal value gives the expected sample value of n and its corresponding t. This method allows us to obtain n with a precision on the third decimal digit and t with a precision of a half micrometer which in our case represents a precision of 0.4%.

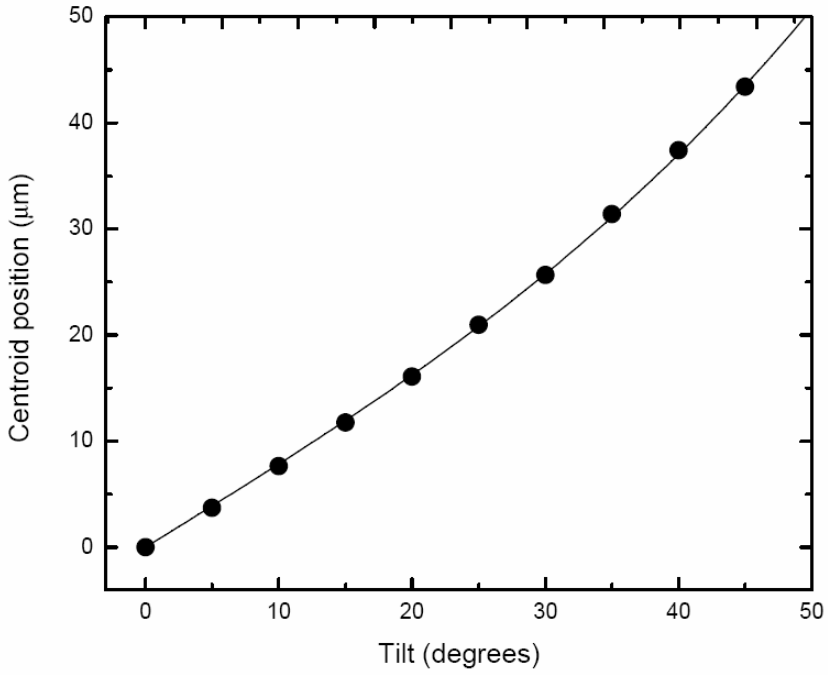

Fig. 5.4. Fitted theoretical curve adjusted to the experimental values (represented by circles).

Our sample consisted of a commercially available cover glass No. 1. The manufacturer sample characteristics compared with those obtained with our technique are given in Table 5.1. The refractive index reported by the manufacturer is only available for $\lambda = 0.589 \mu m$.

	n	$t(\mu m)$
Proposed technique	1.522 ($\lambda = 0.632 \mu m$)	129.6
Reported by manufacturer	1.523 ($\lambda = 0.589 \mu m$)	120-170

Table 5.1. Values for n and t by using our proposed technique compared with the values reported by the manufacturer.

Before finishing this report we want to remark that the sensitivity of the system may be increased by placing the homodyne detector at the best focusing plane in order to measure thinner samples. In contrast, for wider samples a defocus can be intentionally introduced or a larger range PZT can be used.

Chapter 6
Conclusions

With our research we have described and proved analytically and experimentally a technique based on the diffractive properties of Gaussian beams combined with the equations of the transmitted light by a layer to measure locally the geometrical thickness and the refractive index of a transparent pellicle in air, supported only at its border. Under these conditions the pellicle undergoes a continuous piston-like movement making interferometric techniques unfeasible to be used for this purpose. In contrast, we showed that our technique results immune to these movements making it suitable for this application.

To remove ambiguities in the analytical equations due to oscillatory terms we performed the measurements using combinations of neighbor pairs on the region under inspection of the sample allowing us determining their corresponding local geometrical thicknesses and refractive index. This way of measuring can be taken as an advantage because by using different combinations of neighbor pairs, allows to confirm the consistency and correctness of each individual measurement.

Aditionally, by continuing with our research we proposed and proved a technique capable of simultaneously measuring the refractive index and the geometrical thickness of semi-transparent thin optical plates by means of the diffractive properties of a transmitted Gaussian beam. The technique is based on measuring the semi-width of the transmitted beam and the shift of the Gaussian centroid caused by a sample tilt. As the technique is not interferometric, it showed to be robust and immune to external noise. To illustrate the feasibility of the technique we experimentally determined the refractive index and the geometrical thickness of a commercially available cover glass.

Finally it is worth to mention that our research produced four manuscripts which were evaluated and accepted by international journals: two

manuscripts that were published in the journal Applied Optics as author and two manuscripts published in the journal Optics Communications as co-author. Up to date these manuscripts are published and can be found online.

Bibliography

1. J. Park, L. Chen, Q. Wang, and U. Griesmann, "Modified Roberts-Langenbeck test for measuring thickness and refractive index variation of silicon wafers," Opt. Express 20, 20078-20089 (2012).
2. A. Beléndez, T. Beléndez, C. Neipp, and I. Pascual, "Determination of the refractive index and thickness of holographic silver halide materials by use of polarized reflectances," Appl. Opt. 41, 6802-6808 (2002).
3. D. Kim, C. Song, I. Ilev, and J. Kang, "Axial-scanning low-coherence interferometer method for noncontact thickness measurement of biological samples," Appl. Opt. 50, 970-974 (2011).
4. C. Sun, L. Yu, Y. Sun, and Q. Yu, "Scanning white-light interferometer for measurement of the thickness of a transparent oil film on water," Appl. Opt. 44, 5202-5205 (2005).
5. Z. Xu, V. Shilpiekandula, K. Youcef-toumi, and S. Yoon, "White-light scanning interferometer for absolutenano-scale gap thickness measurement," Opt. Express 17, 15104-15117 (2009).
6. K. Moon, N. Kim, J. Shin, Y. Yoon, S. Han, and K. Park, "Continuous-wave terahertz system based on a dual-mode laser for real-time non-contact measurement of thickness and conductivity," Opt. Express 22, 2259-2266 (2014).
7. www.filmetrics.com.
8. W. Vargas and D. Castro, "Closed equation for the normal incidence reflectance of thin films on absorbing substrates," Appl. Opt. 46, 502-505, (2007).
9. C. Wang, J. Lin, H. Jian, and C. Lee, "Transparent thin-film characterization by using differential optical sectioning interference microscopy," Appl. Opt. 46, 7460-7463, (2007).
10. P. Hlubina, D. Ciprian, J. Lunácek, and M. Lesnák, "Dispersive white-light spectral interferometry with absolute phase retrieval to measure thin film," Opt. Express 14, 7678-7685, (2006).

11. Ramsteiner, C. Wild, and J. Wagner, "Interference effects in the Raman scattering intensity from thin films," Appl. Opt. 28, 4017-4023, (1989).
12. Y. Cui and R. Azzam, "Determination of the refractive index and thickness of transparent pellicles by use of the polarization-independent absentee-layer condition," Appl. Opt. 35, 5040-5043, (1996).
13. S. Kim, J. Na, M. Kim, and B. Lee, "Simultaneous measurement of refractive index and thickness by combining low-coherence interferometry and confocal optics," Opt. Express 16, 5516-5526, (2008).
14. Ohmi M, Nishi H, Konishi Y, Yamada Y and Haruna M, “High-speed simultaneous measurement of refractive index and thickness of transparent plates by low-coherence interferometry and confocal optics”, Meas. Sci. Technol. 15 1531-1535, (2004).
15. H. Maruyama, S. Inoue, T. Mitsuyama, M. Ohmi, and M. Haruna, "Low-Coherence Interferometer System for the Simultaneous Measurement of Refractive Index and Thickness," Appl. Opt. 41, 1315-1322, (2002).
16. M. Haruna, M. Ohmi, T. Mitsuyama, H. Tajiri, H. Maruyama, and M. Hashimoto, "Simultaneous measurement of the phase and group indices and the thickness of transparent plates by low-coherence interferometry," Opt. Lett. 23, 966-968, (1998).
17. T. Fukano and I. Yamaguchi, "Simultaneous measurement of thicknesses and refractive indices of multiple layers by a low-coherence confocal interference microscope," Opt. Lett. 21, 1942-1944, (1996).
18. T. Fukano and I. Yamaguchi, "Separation of Measurement of the Refractive Index and the Geometrical Thickness by Use Of A Wavelength-Scanning Interferometer with A Confocal Microscope," Appl. Opt. 38, 4065-4073, (1999).
19. F. Gao, H. Muhamedsalih, and X. Jiang, "Surface and thickness measurement of a transparent film using wavelength scanning interferometry," Opt. Express 20, 21450-21456, (2012).
20. P. de Groot, "Measurement of Transparent Plates with Wavelength-Tuned Phase-Shifting Interferometry," Appl. Opt. 39, 2658-2663, (2000).

21. K. Hibino, B. Oreb, and P. Fairman, "Wavelength-Scanning Interferometry of a Transparent Parallel Plate with Refractive-Index Dispersion," Appl. Opt. 42, 3888-3895, (2003).
22. Coppola, G. ; De Natale, P. ; De Nicola, S. ; Ferraro, P. ; Gioffre, M. ; Iodice, M, “Thickness measurement of thin transparent plates with a broad-band wavelength scanning interferometer”, IEEE Photonics Technology Letters, Vol. 16, No. 5, (2004).
23. Y. Kumar and S. Chatterjee, "Simultaneous determination of refractive index and thickness of moderately thick plane-parallel transparent glass plates using cyclic path optical configuration setup and a lateral shearing interferometer," Appl. Opt. 51, 3533-3537, (2012).
24. Y. Kumar and S. Chatterjee, "Thickness measurement of transparent glass plates using a lateral shearing cyclic path optical configuration setup and polarization phase shifting interferometry," Appl. Opt. 49, 6552-6557, (2010).
25. Joseph W. Goodman, Introduction to Fourier optics, third edition, Roberts & Company Publishers, (2005).
26. M. Cywiak, J. Murakowski, G. Wade, “Beam Blocking Method for Optical Characterization of Surfaces”, Int J Imaging Syst Technol, 11, 164–169, (2000).
27. Joel Cervantes-L, Moisés Cywiak, Octavio Olvera-R, Arquímedes Morales, Defocusing properties of Gaussian beams for measuring refractive index of thin transparent samples, Optics Communications, Volume 309, (2013).
28. Hecht, Eugene, Optics, 2nd Ed, Addison Wesley, 426-431, (1987).
29. Francis A. Jenkins, Harvey E. White, Fundamentals of Optics, 3rd Ed, McGraw-Hill, 260-264, (1957).